

REPORT DOCUMENTATION PAGE				Form Approved OMB No. 0704-0188
<p>Public reporting burden for this collection of information is estimated to average 1 hour per response, including the time for reviewing instructions, searching existing data sources, gathering and maintaining the data needed, and completing and reviewing this collection of information. Send comments regarding this burden estimate or any other aspect of this collection of information, including suggestions for reducing this burden to Department of Defense, Washington Headquarters Services, Directorate for Information Operations and Reports (0704-0188), 1215 Jefferson Davis Highway, Suite 1204, Arlington, VA 22202-4302. Respondents should be aware that notwithstanding any other provision of law, no person shall be subject to any penalty for failing to comply with a collection of information if it does not display a currently valid OMB control number. PLEASE DO NOT RETURN YOUR FORM TO THE ABOVE ADDRESS.</p>				
1. REPORT DATE (DD-MM-YYYY) 31-12-2006	2. REPORT TYPE Final Report	3. DATES COVERED (From - To) 10/01/2003 -12/31/2006		
4. TITLE AND SUBTITLE Optical properties of III-V semiconductor nanostructures and Quantum wells.			5a. CONTRACT NUMBER 5b. GRANT NUMBER FA9550-04-1-0002	
			5c. PROGRAM ELEMENT NUMBER 5d. PROJECT NUMBER 5e. TASK NUMBER 5f. WORK UNIT NUMBER	
6. AUTHOR(S) Omar Manasreh			8. PERFORMING ORGANIZATION REPORT NUMBER	
7. PERFORMING ORGANIZATION NAME(S) AND ADDRESS(ES) Department of Electrical 3217 Bell Engineering Center University of Arkansas Fayetteville, AR 72701			10. SPONSOR/MONITOR'S ACRONYM(S) AFOSR/NE	
9. SPONSORING / MONITORING AGENCY NAME(S) AND ADDRESS(ES) Air Force Office of Scientific Research 875 N. Randolph St., Room 3112 Arlington, VA 22203			11. SPONSOR/MONITOR'S REPORT NUMBER(S) <i>Dr Todd Steinert</i>	
12. DISTRIBUTION / AVAILABILITY STATEMENT <u>Unlimited</u> <i>Distribution Statement: unlimited</i>			AFRL-SR-AR-TR-07-0065	
13. SUPPLEMENTARY NOTE				
14. ABSTRACT <p>We have investigated the optoelectronic applications of interband and intersubband transitions in III-V semiconductors quantum wells and quantum dots. The research efforts included the investigation of intersubband transitions in GaN/AlGaN multiple quantum wells for the 1.3 and 1.5 micron spectral ranges. These wavelengths are important for optical communications. Furthermore, we investigated single wall carbon nanotubes for possible use as space-based solar cell. The final report contains detail discussions of the results obtained during the last three years. At the end of the report, we listed our professional activities including technical papers, books, symposia, invited talks, and students supported by the grant.</p>				
15. SUBJECT TERMS Nanostructures, Long Wavelength Infrared Detectors, Optoelectronic Materials and Devices, III-V semiconductor quantum dots and Quantum Wells.				
16. SECURITY CLASSIFICATION OF: Unclassified		17. LIMITATION OF ABSTRACT None	18. NUMBER OF PAGES	19a. NAME OF RESPONSIBLE PERSON Omar Manasreh
a. REPORT Unclassified	b. ABSTRACT Unclassified	c. THIS PAGE Unclassified		19b. TELEPHONE NUMBER (include area code) (479) 575-6053

FINAL REPORT

OPTICAL PROPERTIES OF III-V SEMICONDUCTOR NANOSTRUCTURE AND QUANTUM WELLS

AFOSR Grant number **F49550-04-1-0002**

Prepared by

Dr. Omar Manasreh

Depart of Electrical Engineering, 3217 Bell Engineering Center,
University of Arkansas, Fayetteville, AR 72701
Phones: Office: (479)575-6053, Mobile: (479) 283-6244,
FAX: (479)575-7967, E-Mails: manasreh@uark.edu

Submitted to

Donald J Silversmith, Ph.D., MBA
Program Manager, Physics and Electronics Directorate
Air Force Office of Scientific Research (AFOSR/NE)
Suite 325/Room 3112
875 North Randolph St.
Arlington, VA 22203-1768
(703) 588-1780
FAX: (703) 696-8481
E-mail: donald.silversmith@afosr.af.mil

DISTRIBUTION STATEMENT A

Approved for Public Release
Distribution Unlimited

TABLE OF CONTENTS

1.	Introduction	4
2.	Broad-band photoresponse from InAs quantum dots embedded into InGaAs graded well...	4
3.	Intersubband Transitions in $\text{In}_{0.3}\text{Ga}_{0.7}\text{As}/\text{GaAs}$ Multiple Quantum Dots of Varying Dot Sizes	8
4.	Intersubband transitions in proton irradiated InGaAs/GaAs multiple quantum dots	13
5.	Intersubband Transitions in $\text{GaN}/\text{Al}_x\text{Ga}_{1-x}\text{N}$ Multi Quantum Wells	16
6.	Determination of the carrier concentration in InGaAsN/GaAs single quantum wells using Raman scattering	21
7.	Longitudinal Modes in $\text{InAlGaAs}/\text{AlGaAs}$ High-Power Laser Diodes	25
8.	List of publications, professional activities and students	31
	A. Papers in technical journals and symposia	31
	B. Books and Symposia	33
	C. Professional Papers at Regional, National, and International Meetings	33
	D. Invited Talks and Presentations.....	34
	E. Students supported by the grant	34

1. Introduction:

Due to the absence of energy-momentum dispersion relation in III-V semiconductor quantum dots, the intersubband transition selection rules that govern the electron-photon interaction are irrelevant. Thus, unlike the selection rules associated with the intersubband transitions in n-type multiple quantum wells, the photons can be absorbed at any light incident angles by the electrons that undergo intersubband transitions in multiple quantum dots. This feature is one of the main attractions of the multiple quantum dots as infrared detectors, since a metallic grading layer is not required, which leads to a more simple device fabrications.

Another attractive feature of the quantum dots is that doping is not required. For an equilibrium steady-state condition, such as optical absorption measurements, the Fermi energy should be above the ground bound state in the quantum dots. Doping in this case is required in order to observe the intersubband transition. On the other hand, doping of quantum dots is not required for the nonequilibrium conditions, such as photoconductivity measurements under the influence of a bias voltage. For the nonequilibrium measurements, quantum dots are populated by the charge carriers that are generated from the contact layers and swept under the influence of the bias voltage.

Furthermore, quantum dots possess a longer lifetime of the excited carriers due to the phonon bottle-neck effect. In order for the quantum dot devices to replace those based on quantum wells, they need to have better performance and perhaps more functionalities. Long wavelength infrared detectors based on intersubband transitions have been sought for their use in space-based focal plane arrays where radiation effects may drastically affect the device performance. Investigation of radiation effects on quantum wells and dots is also important from the semiconductor processing point of view. Many device processing steps rely on the exposure to a variety of particles with energy ranging from a few eV to several MeV. Thus, investigating radiation effects on the intersubband transitions in quantum dots is important for both device processing and performance in harsh environments, such as space.

Several tasks were conducted and some of the results are summarized in the following sections.

2. Broad-band photoresponse from InAs quantum dots embedded into InGaAs graded well

A broad-band photoresponse is obtained from undoped InAs multiple quantum dots grown by the molecular beam epitaxy (MBE) technique on a (100) GaAs substrate. The quantum dots were embedded in an $In_xGa_{1-x}As$ graded well where the *In* mole fraction is chosen in the range of $0.3 \geq x \geq 0.0$. The photoresponse of the reversed biased device, obtained at 80.5 K and using the normal incident configuration, was found to span the spectral range of $3.5 - 9.5 \mu\text{m}$. While the photoresponse is significantly high under the influence of the reverse bias voltage, the forward bias photoresponse is found to be negligible.

In this section, we report on a new broad-band photoresponse results obtained from InAs quantum dots embedded into InGaAs graded well long wavelength infrared photodetector. The broad-band behavior is important features for certain applications, such as hyperspectral and ultra-hyperspectral long wavelength infrared sensors.

The sample grown for the present investigation is an n-i-n structure, which is deposited on a (100) semi-insulating GaAs substrate. A buffer layer made of n-type 0.5 μm GaAs:Si with $[\text{Si}]=1.0\times 10^{18}\text{cm}^{-3}$ and 0.3 μm GaAs:Si with $[\text{Si}]=1.0\times 10^{17}\text{cm}^{-3}$ is grown at the surface of the substrate. 2.2 monolayers (ML) of InAs quantum dots were grown using Stranski-Krastanov mode followed by the growth of a 20 ML graded $\text{In}_x\text{Ga}_{1-x}\text{As}$ well, where x is varied between 0.3 down to zero. A 180 ML GaAs layer is then grown on top of the graded well to form the barrier. The InAs/ $\text{In}_x\text{Ga}_{1-x}\text{As}/\text{GaAs}$ structure is grown at 520 °C and repeated ten times to increase the optical path length. The cap layer is made of 0.4 μm GaAs:Si, where $[\text{Si}]=1.0\times 10^{17}\text{cm}^{-3}$ followed by 0.2 μm GaAs:Si where $[\text{Si}]=1.0\times 10^{18}\text{cm}^{-3}$. The buffer layer was grown at 580 °C while the cap layer was grown at 520 °C. The transformation from two-dimensional to three-dimensional growth mode was monitored by using *in-situ* reflection high-energy electron diffraction. Both the buffer layer and cap layers were used as contact layers. The quantum dot density was estimated from Scanning Tunneling Microscopy images to be on the order of $3.0\times 10^{10}\text{cm}^{-2}$. The average planar area of the quantum dots is $\sim 30\text{nm} \times 30\text{nm}$ and the average height of the dots is ~ 13.5 nm. Mesa structures on the order of $400\mu\text{m} \times 400\mu\text{m}$ were fabricated using wet-etching and photolithography techniques. Gold-germanium alloy metallization pads were deposited on the mesas for wire bonding. For a comparison reason, two InAs quantum dot samples were grown. The structures of these two samples are exactly the same as the sample described above except one sample is embedded in 20 ML $\text{In}_{0.3}\text{Ga}_{0.7}\text{As}$ quantum well and the second sample was grown without any quantum wells. For simplicity, the samples are referred to as InAs dot-graded well, InAs dot-well, and InAs dot. The conduction bands of the three samples are sketched as the insets in Fig. 1.

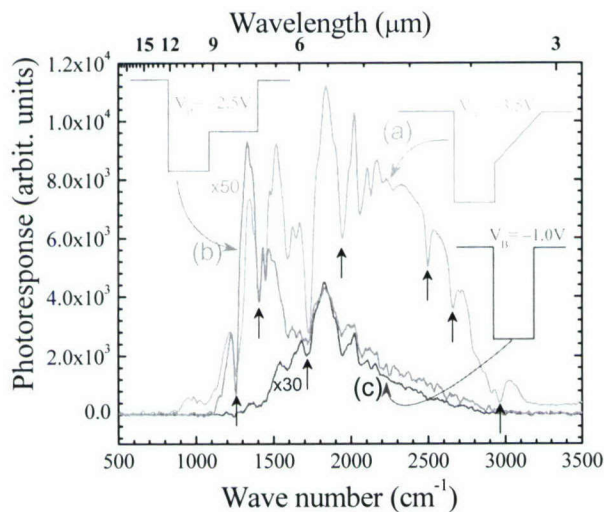


Fig. 1. Photoresponse spectra measured at 80.5K for three different InAs quantum dot structures under the influence of reverse bias voltages. The spectra were obtained for (a) InAs quantum dots embedded into InGaAs graded well device, (b) InAs quantum dots embedded into $\text{In}_{0.3}\text{Ga}_{0.7}\text{As}$ quantum well device ($\times 50$), (c) InAs quantum dots device ($\times 30$), and (d) InAs quantum dots embedded into InGaAs graded well device with a forward bias voltage of +4.0V. The vertical arrows indicate dips that are due to the absorption from the beam-splitter. The insets are sketches of the conduction bands of the three devices.

The photoresponse measurements were made using a BOMEM Fourier-transform infrared spectrometer in conjunction with a continuous flow cryostat. A low-noise current preamplifier Stanford Research System Model SR570 was interfaced with the

spectrometer. The preamplifier was used to both provide a bias voltage and to amplify the device output photocurrent. The measurements were made in the normal incident configuration. The dark current measurements were made at 77K using Keithley 4200-SCS Semiconductor Characterization System.

The photoresponse spectra shown in Fig. 1 were recorded at 80.5 K. Spectrum (a) is obtained for the InAs dot-graded well sample under the influence of a reverse bias voltage of -3.5V. Spectra (b) and (c) were obtained for the InAs dot-well and the InAs dot samples, respectively. The reverse bias voltage of these two samples is indicated in the insets. Spectrum (d) represents the photoresponse of the InAs dot-graded well samples under the influence of the forward bias voltage of +4.0 V. It is clear from this spectrum that a photoresponse is absent. The dips in the spectra that are indicated by the vertical arrows are due to the absorption by the KBr beam-splitter. Spectrum (a) exhibits a rich structure, which is repeatable from device to device fabricated from the same wafer and from run to run. This spectrum covers the spectral range of 3.5 – 9.5 μm with a maximum intensity at about 5.5 μm . For a comparison reason, the photoresponse of the InAs dot-well and InAs dot devices were multiplied by 30 and 50, respectively. Since the light source used in the spectrometer is not calibrated, the unit of the photoresponse is taken as an arbitrary unit. With a calibrated light source, one can obtain the responsivity, which is a figure of merit in units of A/W. An accurate estimate of another figure of merit, the detectivity, in this case was difficult to obtain since the power of the light source was too weak to measure. However, if one uses the following expression for n-type quantum well infrared photodetectors

$$D^* = 1.1 \times 10^6 e^{E_c/(2kT)} \text{ cm}\sqrt{\text{Hz}} / W \quad (1)$$

where E_c is the cutoff energy, k is Boltzmann constant, and T is temperature, then the detectivity is calculated to be on the order of $1.34 \times 10^{10} \text{ cm}\sqrt{\text{Hz}} / W$. This value is obtained for $T=80.5\text{K}$ and $E_c=130.5 \text{ meV}$ ($9.5 \mu\text{m}$). Notice that the empirical expression of D^* given by (1) depends solely on the temperature and the cut-off energy. It may not be applicable to quantum dot detectors, but it is useful for comparison when the light source is not calibrated.

A remarkable feature of the photoresponse shown in Fig. 1 is the broad feature of the photoresponse obtained for the InAs-graded well sample where the full width at half maximum spans $\sim 4 \mu\text{m}$ and $\Delta\lambda/\lambda \sim 0.7$. The broad band behavior is an important feature for certain applications, such as hyperspectral and ultra-hyperspectral long wavelength infrared sensors.

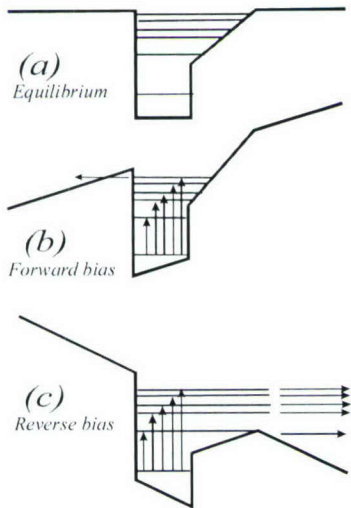


Fig. 2. A sketch of the conduction band of the InAs dot-graded well structure is shown at (a) zero bias, (b) forward bias, and (c) reverse bias. Several energy levels are indicated. The vertical arrows represent the transitions from the ground to the excited states due to the photon absorption. The horizontal arrows represent the transport of the photoexcited carriers.

The quantum dot structure of the InAs dot-graded well used in the present investigation is designed such that the InAs quantum dots are embedded in graded InGaAs quantum wells to produce InAs/InGaAs/GaAs quantum dot structures as shown in Fig. 2 (a). The photoresponse spectra (d) and (a) shown in Fig. 1, can be explained by examining the conduction band structure sketched in Fig. 2 (b) and (c) for applied forward and reverse bias voltage, respectively. Several energy levels are also shown in this figure. When a forward bias voltage is applied, the conduction band alignment takes the shape shown in Fig. 2 (b). The quantized energy levels are still bound and the photoexcited carriers need to tunnel through the barrier in order for them to contribute to the photocurrent and photoresponse of the detector. Experimentally, a photoresponse under the influence of the forward bias voltage is found to be below the detection level and could not be observed [see Fig. 1 spectrum (d)]. This model suggests that a low tunneling probability due to the thick barrier is the reason for the absence of the photoresponse. When the sample is reversed biased, the excited states are resonant in the continuum as shown in Fig. 2 (c) and the measured photoresponse is quite strong as shown in Fig. 1 spectrum (a). This is due to the fact that the photoexcited charge carriers (depicted by the vertical arrows) are swept under the influence of the reverse bias voltage without encountering any barriers as indicated by the horizontal arrows. Thus, the rich structure observed in Fig. 1 spectrum (a) is due to various transitions from the ground state to the excited states.

The dark currents of the InAs dot, InAs dot-graded well, and InAs dot-well samples were measured at 77K and plotted in Fig. 3 as curves (a), (b), and (c), respectively. For high reverse bias voltages, the dark currents of the InAs dot and InAs dot-well samples are higher than that of the InAs dot-graded well sample. The implication of this observation is that devices from the InAs dot and InAs dot-well samples operate at lower reverse bias voltages.

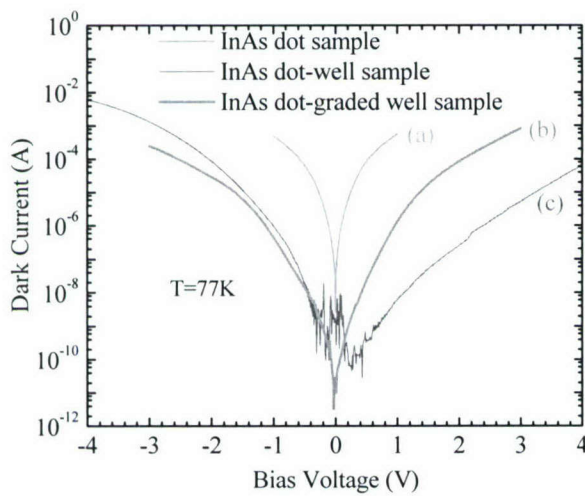


Fig. 3. The dark currents of photodetector devices measured at 77 K as a function of the bias voltage. The curves are obtained for (a) InAs quantum dots device, (b) for the InAs quantum dots embedded into InGaAs graded well device, and (c) is recorded for an InAs quantum dots embedded into $In_{0.3}Ga_{0.7}As$ quantum well device.

In conclusion, a normal incident broad band photoresponse was measured for InAs quantum dots embedded in a graded $In_xGa_{1-x}As$ quantum well with GaAs barriers.

The photoresponse is observed only when the sample is reverse-biased. The forward-bias configuration did not yield a measurable signal. The rich structure observed in the photoresponse is attributed to the electronic transitions between the ground states and

several excited states. The absence of the photoresponse under the forward bias voltage is explained by a model where the excited states remain bound and the electron tunneling probability is too small.

3. Intersubband Transitions in $\text{In}_{0.3}\text{Ga}_{0.7}\text{As}/\text{GaAs}$ Multiple Quantum Dots of Varying Dot-Sizes

We investigate the optical absorption spectra of intersubband transitions in $\text{In}_{0.3}\text{Ga}_{0.7}\text{As}/\text{GaAs}$ multiple quantum dots (MQDs) grown by molecular beam epitaxy. By varying the number of $\text{In}_{0.3}\text{Ga}_{0.7}\text{As}$ monolayers deposited, a series of samples with varying dot sizes ranging from 10 – 50 monolayers were obtained. The quantum dots grown with size less than 15 monolayers or more than 50 monolayers did not yield any observable measurements of intersubband transition. This suggests that there exist a critical upper and lower limit of $\text{In}_{0.3}\text{Ga}_{0.7}\text{As}$ quantum dots for infrared detectors. A wavelength range of 8.60 – 13.70 μm is achieved for structures grown with the above monolayers range. The theoretical line-shape of the intersubband transition absorption was compared to the experimental measurements. From the lineshape, it was deduced that bound-to-continuum transition is present in thick quantum dots and bound-to-bound transition is present in thinly grown quantum dots.

The most extensively used material systems for infrared imaging is the II-VI semiconductor, HgCdTe. Although this material possesses a very high quantum efficiency and detectivity, it suffers from manufacturing related problems. Apart from being difficult to grow and process, the material itself is very costly compared to the III-V semiconductors. The technology for producing HgCdTe detectors is not yet mature enough to achieve uniformity over large areas and allow for reliable reproduction. These obstacles lead to low yields and high detector costs.

These disadvantages lead many researchers to seek out an alternative solution which eventually lead to the birth of the quantum well infrared photodetector (QWIP). Quantum well infrared photodetectors are designed from wide bandgap (III-V) semiconductor materials in such a way where quantum confinement is created. Unlike HgCdTe which utilizes electronic transitions across the fundamental bandgap, QWIPs relies on transitions between two or more bound energy levels within quantum wells. This extends the range of infrared sensing to the far infrared. The material growth and fabrication technology of III-V based devices are more attainable as compared to these based on II-VI group. However, the QWIP has several limitations such as the insensitivity to normal incidence radiation. Photons incident normal to the structure are not absorbed due to selection rules associated with intersubband transitions. Special grating layers must be etched onto the top contact layer of the structure to scatter incident photons at an angle into the structure.

In recent years, a more novel structure based on quantum dots has shown a reasonable success for infrared detection. One of the main attractions for quantum dots based detectors is their intrinsic ability to absorb light at the normal incidence. Sensitivity at the normal incidence would simplify device fabrication and reduces costs. This technology is still at its infancy and thus merits further investigation. In this article, we report on the optical absorption of intersubband transitions in $\text{In}_{0.3}\text{Ga}_{0.7}\text{As}/\text{GaAs}$ multiple quantum dots. The peak position energy and intensity of these transitions were

investigated as a function of monolayers of $\text{In}_{0.3}\text{Ga}_{0.7}\text{As}$ quantum dots. The optical absorption measurements were performed in the waveguide configuration.

The quantum dot structures were grown by molecular-beam-epitaxy (MBE) using Stranski-Krastanow growth mode on semi-insulating GaAs (100) substrates. After loading the substrate in the MBE growth chamber, the substrate was heated to 600°C in As atmosphere to allow the desorption of the oxide layer. During the MBE growth, the As beam equivalent pressure was kept constant at 1×10^{-5} Torr for all samples. Subsequently, a 0.5 μm Si-doped GaAs buffer layer, which also serves as a contact layer, was deposited at the above mentioned substrate temperature. The substrate was then cooled down to 500°C and 30 periods of $\text{In}_{0.3}\text{Ga}_{0.7}\text{As}/\text{GaAs}$ quantum dots were grown.

The growth was monitored by an *in situ* reflection high-energy electron diffraction (RHEED). A 0.5 μm Si-doped GaAs contact layer was deposited at the top of the structure after increasing the substrate temperature to 580°C. A series of sample with different $\text{In}_{0.3}\text{Ga}_{0.7}\text{As}$ thicknesses ranging from 15 – 50 monolayers were grown. The transition from a layer-by-layer growth mode to three-dimensional islanding occurs at 10 monolayers of $\text{In}_{0.3}\text{Ga}_{0.7}\text{As}$ as judged from the point at which the RHEED patterns transformed from being streaky to spotty. The $\text{In}_{0.3}\text{Ga}_{0.7}\text{As}$ quantum dots were doped with $[\text{Si}] \sim 1 \times 10^{11} \text{ cm}^{-2}$, while the buffer and cap layers were doped with $[\text{Si}] \sim 1 \times 10^{18} \text{ cm}^{-3}$.

The thickness of the GaAs barrier layer was 120 monolayers for all samples. The structure is schematically shown in Fig. 1.

The samples were placed in a continuous flow cryostat and characterized using a Bomem DA8 Fourier Transform Infrared (FTIR) Spectrometer. The measurements were performed in the waveguide configuration. This configuration allows the light to make multiple passes through the sample which increases the net intersubband absorption significantly and permits accurate analysis of the results [Fig. 2(a)]. The waveguide geometry was fabricated by cutting the samples into sizes of 2.5mm x 7mm x 0.6mm with the beveled facet being polished at a 45° angle. A scanning electron microscope (SEM) image of the waveguide is depicted in Fig. 2(b). The optical absorption spectra were measured at room temperature and at liquid nitrogen temperature (77K).

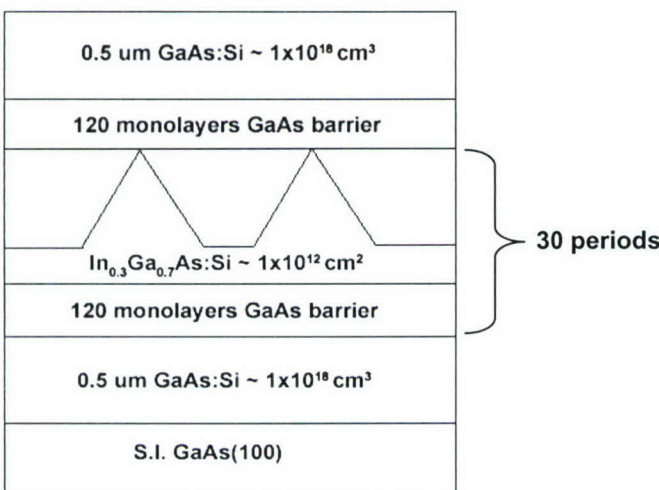


Fig. 1. A schematics of $\text{In}_{0.3}\text{Ga}_{0.7}\text{As}/\text{GaAs}$ multiple quantum dot structures

a)

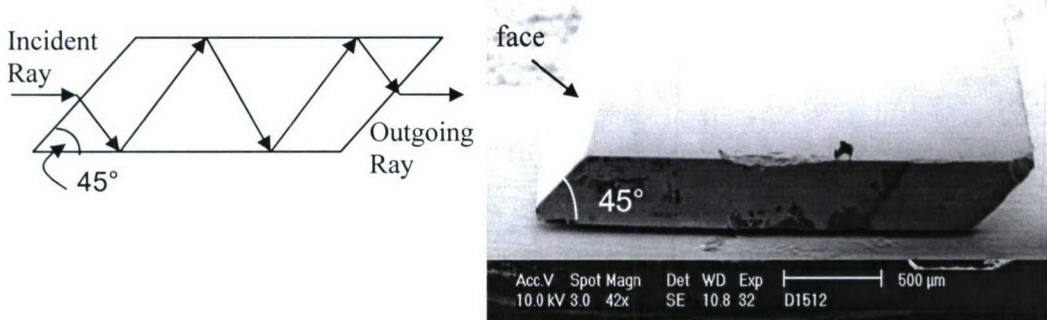


Fig. 2. a) A scanning electron microscope image of a sample cut and polished into waveguide geometry and b) light enters through the face at a 45° angle and makes several passes through the sample before exiting.

A wavelength range of $8.60 - 13.70 \mu\text{m}$ is achieved for structures grown ranging from 15 to 50 MLs of $\text{In}_{0.3}\text{Ga}_{0.7}\text{As}/\text{GaAs}$ multiple quantum dots. The optical absorption spectra of the intersubband transitions for seven samples are shown in Fig. 3. It is noted that as the monolayers of deposited $\text{In}_{0.3}\text{Ga}_{0.7}\text{As}$ increased, the peak position wavelengths of the intersubband transitions is red-shifted. The experimental measurements were then compared with the theoretical results. In our case, the intersubband transitions shown in Fig. 4 have a finite width; this implies that there is a distribution of different dot sizes in the quantum dot layers in addition to other broadening mechanisms such as phonon broadening.

The line shape of the optical absorption spectra of samples ranging from 20 – 50 MLs takes the form of a Lorentzian function. This suggests that the transition is a bound-to-bound transition depicted in Figure 4(a) where E_0 and E_1 are the ground and excited states, respectively. The sample with 15 MLs of $\text{In}_{0.3}\text{Ga}_{0.7}\text{As}$ [spectrum (a) in Fig. 3] was found not to possess a Lorentzian line shape. Instead, its line shape is asymmetrical and resembles those observed in bound-to-continuum transitions [depicted in Fig. 4(b)] in multiple quantum wells. A bound-to-continuum transition occurs when the electrons are excited from the ground state, E_0 , to the first excited state depicted as E_1 which resides in the continuum of the conduction band.

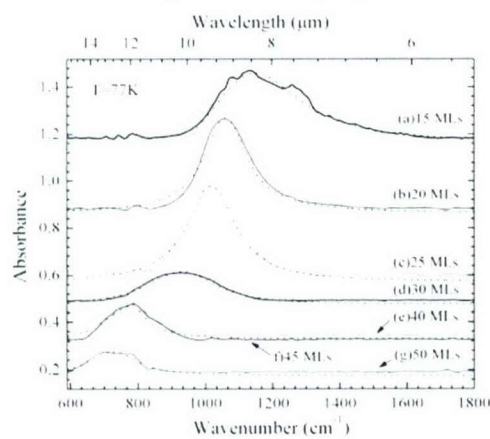


Fig. 3. Optical absorption spectra of the intersubband transitions for seven samples grown with different quantum dot sizes measured at 77K. The theoretical curves are shown in dotted lines.

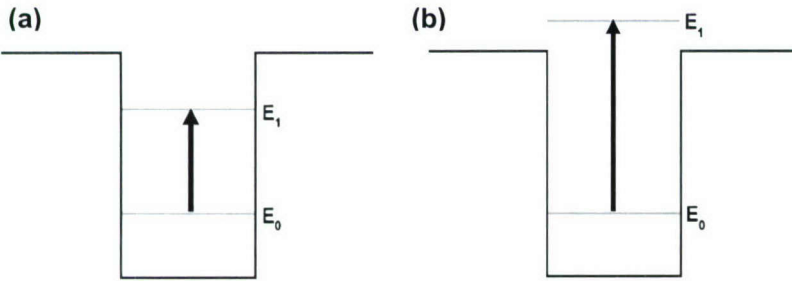


Fig. 4. Schematics of bound states in the quantum dots shown as E_0 and E_1 . (a) A bound-to-bound transition and (b) a bound-to-continuum transition.

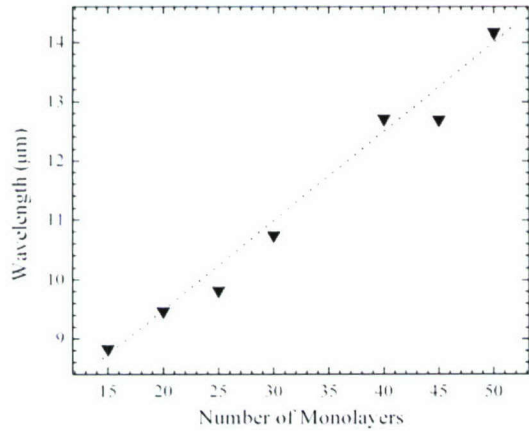


Fig. 5. The peak position of the intersubband transitions measured at 77K plotted as a function of the number of $\text{In}_{0.3}\text{Ga}_{0.7}\text{As}$ MLs deposited. The dotted line is drawn to demonstrate the linearity.

The wavelengths associated with the peak positions of the intersubband transition spectra were found to increase linearly as the number of deposited $\text{In}_{0.3}\text{Ga}_{0.7}\text{As}$ MLs are increased as shown in Fig. 5. The intensity of the intersubband

transitions obtained from integrating the area under the curve is shown to decrease as the quantum dot size increased. This result is shown in Table I. The decreased intensity could be due to the introduction of dislocations that causes degradation at the interface as well as degradation in the quantum dots themselves.

In addition to the optical absorption, photoluminescence (PL) measurements were obtained for a few multiple quantum dot samples. The PL peak position is shown in Fig. 6 as a function of deposited $\text{In}_{0.3}\text{Ga}_{0.7}\text{As}$ MLs. The spectra were measured at 77K with a 532 nm high power green laser having an excitation power of 25 mW. As expected, the PL intensity is relatively weaker in the sample having its excited state residing in the continuum [Fig. 6(a)] than the samples with bound excited states [Fig. 6(b) and (c)]. The narrow spectral width of samples (a) – (c) in Fig. 6 indicates the high uniformity of the quantum dots.

It is noted that samples larger than 30 MLs did not yield any observable photoluminescence from the quantum dots. Peaks observed at $\sim 11,500 \text{ cm}^{-1}$ in the samples with 25 MLs and 30 MLs [Fig. 6(c) and (d)] comes from the two-dimensional “wetting layer”. This “wetting layer” is a resultant of the Stranski-Krastanow growth mode which causes degradation of the quantum dots. These defects may act as traps and non-radiative recombination centers for carriers which can explain the weaker absorption

intensity and non-observable luminescence from samples having larger than 30 MLs of deposited $In_{0.3}Ga_{0.7}As$.

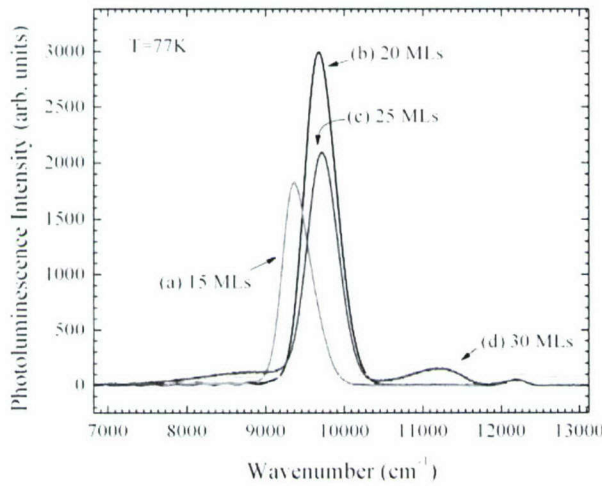


Fig. 6. The photoluminescence spectra of quantum dot samples ranging from 15 – 30 MLs of $In_{0.3}Ga_{0.7}As$ measured at 77K.

Table I. Intensity of the intersubband transitions measured at 77K as a function of integrated area under the curve. As the quantum dot sizes increased (increasing number of monolayers), the intensity decreased.

Number Monolayers	of T=77K	Integrated Area (arb. units)
15		101.02
20		76.40
25		78.43
30		30.70
40		24.83
45		25.10
50		14.51

In conclusion, by varying the quantum dot size alone we were able to “tune” the peak wavelength towards the far IR. Quantum dots grown with sizes less than 15 monolayers did not show any observable intersubband transitions. This suggests that there exist a critical lower limit for quantum confinement. As the quantum dot sizes increased up to 50 monolayers, the observed intersubband transitions showed significant decrease in the intensity implying that it is the upper limit that yields observable measurements. Despite the decreased intersubband intensity, these results are promising as there are other design parameters that could be adjusted to enhance the signal or advance the peak wavelengths beyond 14 μm . These include varying growth conditions,

changing doping levels in the quantum dots, increasing the uniformity of quantum dot sizes and modifying structure designs.

4. Intersubband transitions in proton irradiated InGaAs/GaAs multiple quantum dots

This section is focused on the proton irradiation effect on 3 MeV proton irradiation effect on the optical absorbance properties of the intersubband transitions in $\text{In}_{0.3}\text{Ga}_{0.7}\text{As}/\text{GaAs}$ multiple quantum dots grown on semi-insulating (001) GaAs substrate. The intensities of the absorbance spectra were investigated as a function of irradiation dose. Post-irradiation thermal annealing was performed on a sample in which the intersubband transition was completely depleted when the sample was subject to an irradiation dose of $5 \times 10^{14} \text{ cm}^{-2}$. Unlike the thermal recovery of the intersubband transition reported for multiple quantum wells, thermal annealing recovery of the depleted intersubband transitions in the multiple quantum dots was not observed. The intensity of the intersubband transition in the quantum dots as a function of irradiation dose is compared to those observed in proton irradiated $\text{GaAs}/\text{Al}_{0.3}\text{Ga}_{0.7}\text{As}$ and $\text{In}_{0.52}\text{Ga}_{0.48}\text{As}/\text{In}_{0.52}\text{Al}_{0.48}\text{As}$ multiple quantum wells.

A 30-period $\text{In}_{0.3}\text{Ga}_{0.7}\text{As}/\text{GaAs}$ multiple quantum dots wafer was grown by a molecular beam epitaxy (MBE) technique on a semi-insulating (001) GaAs substrate. The growth was monitored by an *in-situ* reflection high-energy electron diffraction (RHEED) instrument. The deposited number of monolayers of the $\text{In}_{0.3}\text{Ga}_{0.7}\text{As}$ is 25. The transition from a layer-by-layer growth mode to three-dimensional islanding occurs at 10 monolayers of $\text{In}_{0.3}\text{Ga}_{0.7}\text{As}$ as judged from the point at which the RHEED patterns transformed from being streaky to being spotty. The $\text{In}_{0.3}\text{Ga}_{0.7}\text{As}$ quantum dots were doped with $[\text{Si}] \sim 1 \times 10^{11} \text{ cm}^{-2}$ in order to populate the quantum dots with electrons. The density of the quantum dots was estimated to be on the order of 10^{11} cm^{-2} . The multiple quantum well samples were also grown by the MBE technique. The optical absorption spectra were recorded using a BOMEM DA8 spectrometer in conjunction with a continuous flow cryostat. The samples were cut into a waveguide geometry with the facet being polished at 45° similar to those waveguides reported earlier. Furnace thermal annealing was performed in a continuous flow of Argon gas at 500°C . Several samples cut from the same wafer were irradiated with different doses of 3 MeV protons.

The absorbance spectra of the intersubband transition in $\text{In}_{0.3}\text{Ga}_{0.7}\text{As}/\text{GaAs}$ multiple quantum dot samples were measured at room temperature using the waveguide configuration. The results are displayed in Fig. 1 for five multiple quantum dot samples irradiated under different conditions. The intensity of the intersubband transition decreases as the 3 MeV proton dose is increased. As the spectrum indicates, the transition in the sample irradiated with a dose of $5 \times 10^{14} \text{ cm}^{-2}$ is completely depleted.

The relative intensity of the intersubband transitions in the $\text{In}_{0.3}\text{Ga}_{0.7}\text{As}/\text{GaAs}$ multiple quantum dots is plotted in Fig. 2 as a function of irradiation dose. For a comparison reason, the relative intensities of the intersubband transitions as a function of irradiation dose in 55\AA $\text{In}_{0.52}\text{Ga}_{0.48}\text{As}/300\text{\AA}$ $\text{In}_{0.52}\text{Al}_{0.48}\text{As}$ multiple quantum well samples (50 period) and 75\AA $\text{GaAs}/100\text{\AA}$ $\text{Al}_{0.3}\text{Ga}_{0.7}\text{As}$ multiple quantum well samples (50 period) are shown in the figure. Protons of energy 1 MeV were used to irradiate the multiple quantum well samples. The 1 MeV proton doses, however, were scaled to those of the 3 MeV protons used to irradiate the multiple quantum dot samples by using an established technique involving the comparison of each particles nonionizing energy loss. The

scaling factor was determined to be 2.65, which is the ratio between the damage factors for the 1 MeV and 3 MeV protons.

Fig. 1. Absorbance spectra of the intersubband transition in 3 MeV proton irradiated $In_{0.3}Ga_{0.7}As/GaAs$ multiple quantum dot samples. The spectra were obtained at room temperature after the samples were irradiated with different doses.

It is clear from Fig. 2 that the radiation tolerance of $In_{0.3}Ga_{0.7}As/GaAs$ multiple quantum dots is comparable to that of the $GaAs/Al_{0.3}Ga_{0.7}As$ multiple quantum wells. On the other hand, $In_{0.52}Ga_{0.48}As/In_{0.52}Al_{0.48}As$ multiple quantum well samples withstood proton irradiation by more than an order of magnitude as compared to the multiple quantum dots samples. One can also notice that the relative intensity of the intersubband transition in the multiple quantum dot samples remains higher than that of the $GaAs/Al_{0.3}Ga_{0.7}As$ multiple quantum well samples for doses less than $5 \times 10^{13} \text{ cm}^{-2}$.

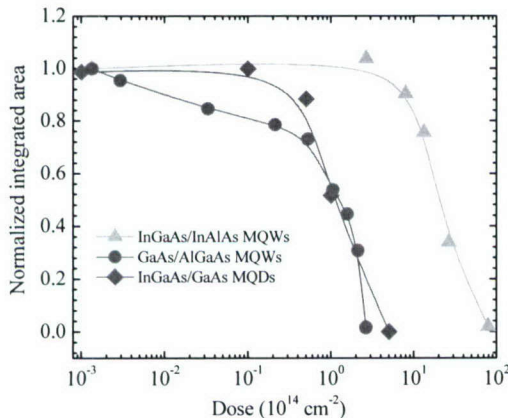
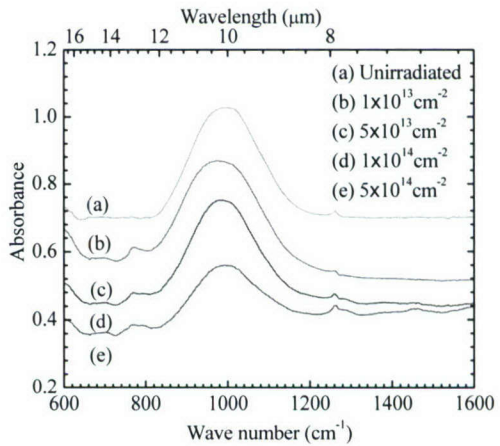


Fig. 2. The normalized integrated area of the intersubband transition as a function of irradiation dose obtained for $In_{0.3}Ga_{0.7}As/GaAs$ multiple quantum dot samples (diamonds), $In_{0.52}Ga_{0.48}As/In_{0.52}Al_{0.48}As$ multiple quantum well samples (triangles) and a $GaAs/Al_{0.3}Ga_{0.7}As$ multiple quantum well samples (circles).

Thermal annealing recovery of the depleted intersubband transitions in heavily irradiated multiple quantum

well samples was observed. In the case of the $In_{0.3}Ga_{0.7}As/GaAs$ multiple quantum dot samples, the depleted intersubband transition was not recovered. Instead, a broad-band in the absorbance spectrum with an integrated area about five times larger than that of the intersubband transition in the control sample (unirradiated) is observed after annealing the heavily irradiated quantum dot sample at 500 °C for 15 and 30 min. The results are shown in Fig. 3. Spectrum (a) was obtained for the quantum dot sample after it was irradiated to a fluence of $5 \times 10^{14} \text{ cm}^{-2}$ and before thermal annealing. Spectra (b) and (c) were obtained after annealing the irradiated sample at 15 and 30 min, respectively. The broad-band, shown in Fig. 3, peaks at $\sim 5.0 \mu\text{m}$ (248 meV) while the intersubband

transition in the control sample peaks at $\sim 10 \mu\text{m}$ (124 meV) giving rise to a large energy blueshift, which is not a characteristic behavior of intersubband transitions in quantum wells and dots.

Another argument that does not support the broad-band as being an intersubband transition is presented in Fig. 4. The spectra plotted in this figure were recorded for an unirradiated multiple quantum dots sample that was subject to annealing conditions similar to those applied to the sample irradiated with $5 \times 10^{14} \text{ cm}^{-2}$. Spectrum (a) is obtained before thermal annealing while spectra (b) and (c) were obtained after annealing the sample at 500°C for 15 and 30 min, respectively. The intersubband transition is completely depleted after annealing the sample for 30 min as shown in spectrum (c).

The intersubband transition remains depleted in the control sample upon further annealing for 45 min at 500°C and for 30 min at 600°C . On the other hand, the broad-band observed in the heavily irradiated sample after annealing, shown in Fig. 3, was not affected when the annealing temperature was increased to 600°C . Thus, the broad-band observed in spectra (b) and (c) of Fig. 3 is most likely related to irradiation-induced defects.

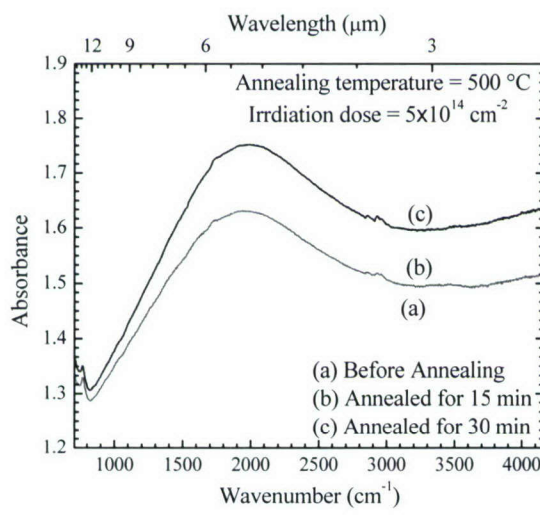
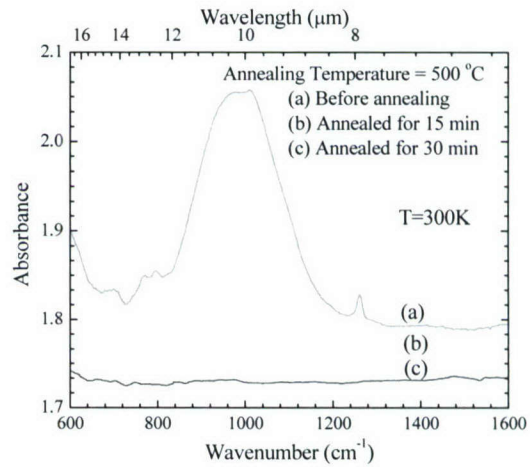


Fig. 3. Absorbance spectra obtained for a sample irradiated to a fluence of $5 \times 10^{14} \text{ cm}^{-2}$. Spectrum (a) was obtained after irradiation and before furnace thermal annealing, spectrum (b) was obtained after irradiation and after thermal annealing the sample at 500°C for 15 min, and spectrum (c) was obtained after irradiation and after thermal annealing the sample at 500°C for 30 min.

Fig. 4. Thermal annealing effect on the absorbance of the intersubband transition in the control sample (unirradiated). Spectrum (a) was obtained before thermal annealing, spectrum (b) was obtained after thermal annealing the sample at 500°C for 15 min, and spectrum (c) was obtained after thermal annealing the sample at 500°C for 30 min.

The atomic structure of this defect is difficult to determine, but the high annealing temperature suggests that this defect cannot be a vacancy or an interstitial



defect. It is most likely related to an antisite-related complex defect since this class of defects is thermally stable at elevated temperatures. Light scattering from irradiation-induced dislocations is another possible explanation to the presence of the broad peak.

In conclusion, the optical absorbance of the intersubband transition in proton irradiated InGaAs/GaAs multiple quantum dot samples is investigated as a function of irradiation dose and furnace thermal annealing. The intensity of the intersubband transition was observed to decrease as the dose is increased and the transition was completely depleted in a sample irradiated to a fluence of $5 \times 10^{14} \text{ cm}^{-2}$. The behavior of the intersubband transition relative intensity as a function of irradiation dose is similar to that of the intersubband transition observed in GaAs/AlGaAs quantum well samples. Thermal annealing recovery of the depleted intersubband transition in a heavily irradiated multiple quantum dots sample was not observed. Instead, a broad-band was observed after annealing the sample. This broad-band does not possess the characteristic of intersubband transitions in quantum dots and quantum wells, suggesting that it may be related to irradiation-induced defects or dislocations.

5. Intersubband Transitions in $\text{GaN}/\text{Al}_x\text{Ga}_{1-x}\text{N}$ Multi Quantum Wells

Intersubband transitions (ISTs) in $\text{GaN}/\text{Al}_x\text{Ga}_{1-x}\text{N}$ multiple quantum wells (MQWs) were investigated using an optical absorption technique. Several samples were grown by either Molecular Beam Epitaxy (MBE) or Metal-Organic Chemical Vapor Deposition (MOCVD) and were investigated using both normal incident and waveguide configurations. The waveguides were fabricated by dicing each sample into 2 mm wide by 5 mm long pieces with two facets polished at 45 degrees with respect to the surface such that light propagates across the sample's width. Preliminary results indicate that ISTs are observable in Si-doped and undoped $\text{GaN}/\text{Al}_x\text{Ga}_{1-x}\text{N}$ MQWs. The source of these charge carriers in the undoped samples are explained as being due to the spontaneous polarization effect which exists at the $\text{GaN}/\text{Al}_x\text{Ga}_{1-x}\text{N}$ interfaces where the GaN surface has Ga-polarity. Scanning Electron Microscopy indicates that a sample containing what appeared to be a large number of cracks and or hexagonal voids lacked the presence of ISTs.

There has been much consideration given to III-nitride semiconductors in optical devices due to the availability of direct bandgaps ranging from 0.7 eV for InN to 6.1 eV for AlN. The insertion of the lower bandgap GaN material between two layers of larger bandgap ternary $\text{Al}_x\text{Ga}_{1-x}\text{N}$ alloy gives rise to a quantum well structure whose periodicity can be utilized to create MQWs of $\text{Al}_x\text{Ga}_{1-x}\text{N}/\text{GaN}$. These MQWs structures could be tuned by varying the aluminum content, doping, well parameters, and barrier parameters to cover a multitude of wavelengths for detector applications. While these transitions have been well documented, mainly in AlGaAs/GaAs quantum structures in the subsequent years, there has been only recent attention given to $\text{Al}_x\text{Ga}_{1-x}\text{N}/\text{GaN}$ MQWs particularly for the communication wavelength of 1.55 μm . Inherent properties of nitride semiconductors such as large electron effective mass ($m^* \sim 0.2\text{-}0.3m_0$), large LO phonon energy ($E_{\text{LO}} \sim 91 \text{ meV}$), large conduction band offsets, and fast IST relaxation times ($\sim 150\text{-}370 \text{ fs}$) make GaN based nitride semiconductors an ideal contender for high speed detectors. Growth related issues attributed to lattice mismatch of sapphire (Aluminum Oxide) and GaN ($\approx 13\%$) have continued to plague the growth of low defect density

materials. Interests in the notion that these quantum well structures could provide the next generation of detectors operating at the communication wavelength of 1.55 μm have driven the need to further understand the obstacles limiting the growth of this material.

In this section, we report the observation of ISTs in GaN/ $\text{Al}_x\text{Ga}_{1-x}\text{N}$ MQW structures grown by both MOCVD and MBE on c-plane (0001) sapphire substrates. GaN/ $\text{Al}_x\text{Ga}_{1-x}\text{N}$ MQW structures using an optical absorption technique. For the absorption experiments, the fabrication of waveguides was necessary to increase the absorption optical length of the photon, since this configuration enables multiple passes of light inside the sample. Images of the samples obtained using Scanning Electron Microscopy (SEM) were inspected to determine the surface morphology.

The optical absorption spectra were recorded using waveguide, Brewster's angle, and normal incident configurations. However, only the results obtained from the waveguide configuration is reported in this paper. The samples under investigation consisted of both Si doped and undoped GaN wells. Since absorption in n-type quantum well structures occurs only for polarization parallel to the growth axis and is forbidden under normal incidence, the waveguide configuration is used to enhance the absorption of photons in the sample taking advantage of multiple passes of light. In preparation for waveguide measurements, samples were fabricated into waveguides by cutting a 5mm long by 2mm wide piece from each wafer. Using various grades of lapping material, the waveguide with 45 degree facets were formed and polished (see Fig. 1) such that light could propagate across its width.

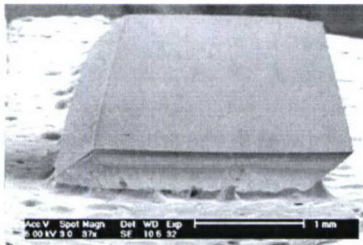


Fig 1: SEM image of a fabricated waveguide.

A specially designed sample holder was used to house the waveguide in the cryostat during absorption measurements such that light could be incident upon the 45 degree facet. A Mercury Cadmium Telluride detector was used in conjunction with a Potassium Bromide beam splitter to investigate the intersubband absorption in the range of 1.43-25 μm . The absorption spectra were recorded at either 300 K or 77K using a continuous flow cryostat.

Six samples grown by either the MBE or MOCVD techniques are used in the present investigation. The MBE grown samples are labeled 1293, 1297, and 1300, while the MOCVD grown samples are labeled 1142, 1144, and 1145. The structures of these samples are presented in Table I. The samples were chosen to show the variation of the results in diverse sample structures. While there was successful observation of ISTs in several samples, it was noted that many samples do not possess ISTs, which is an indication of difficult growth conditions. As an example, the absorbance spectra of the IST obtained for four samples of GaN/ $\text{Al}_x\text{Ga}_{1-x}\text{N}$ MQWs recorded at room temperature are displayed in Fig.2, The structure observed at approximately 3.4 μm is due to absorption from C-H vibrational modes. Variations seen in Table I between structures

1293, 1297, 1300, and 1144 give rise to absorption at different wavelengths. These different wavelengths, peak intensities, and spectral line widths are due to factors such as well width and the corresponding position of these upper states from the top of the barrier.

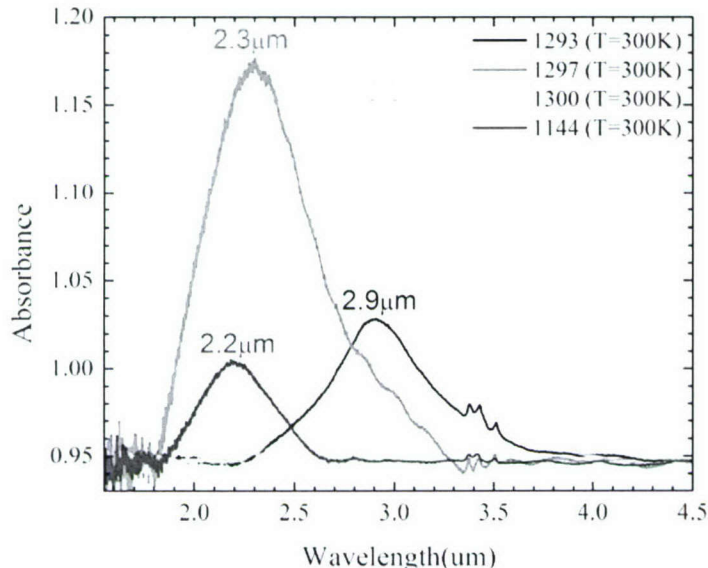


Fig 2: Intersubband Transitions observed at 2.2, 2.3, 2.9, and 3.0 μm in an MOCVD grown sample labeled 114, and MBE grown samples labeled 1297, 1293, and 1300. The well thickness of the samples are, 3.5, 1.0, 1.0, and 1.0 nm, respectively.

Although measurements were conducted for all structures listed in Table I, samples 1142 and 1145 did not exhibit any absorption properties (i.e., lack ISTs). The well widths shown in table I are the projected thicknesses, but it does not mean that the actual growth rate yield the exact thicknesses shown in this table. The results in Fig. 2, however indicates that the actual growth rate is quite different from the project thicknesses. In both MBE and MOCVD reactors, the growth rate appears to be off target. Thus, additional calibration is underway to pinpoint the growth conditions of III-nitride quantum well structures. We also noted that the intensity of the IST does not follow the dopant concentration due to the fact that the spontaneous polarization induced charges play a major role in the density of the 2-dimensional electron gas formed in the well. The investigation of this topic is outside the scope of the present paper. While SEM provides information on the surface morphology of the MQW structures, this technique does allow one to investigate the microscopic structures of the samples. Tunneling electron microscopy is more appropriate for obtaining information at the atomic scale. However, we attempt to characterize the surface of the six samples investigated here using the SEM technique so as to observe if surface morphology played a limiting role in the optical properties of each material. Initial efforts were focused on samples 1142, 1144, and 1145 since ISTs had only been observed in one of these MOCVD grown samples as seen in Fig.2.

Table I: Layer by layer description of each of the structures.

1142		1144	
0.2 um GaN: Si ~1x10^-18		0.2 um GaN: Si ~1x10^-18	
10 nm AlGaN-30% Al	x30	10 nm AlGaN-30% Al	x30
3.5 nm GaN: Si ~1x10^-18		3.5 nm GaN: Si ~1x10^-18	
13 nm AlN		13 nm AlN	
0.5 um GaN: Si ~1x10^-18		0.5 um GaN: Si ~1x10^-18	
1.2 GaN Template		0.5 AlN Template	
C-plane (0001) Sapphire		C-plane (0001) Sapphire	
1145		1293	
0.2 um GaN: Si ~1x10^-18		10 nm GaN: Si ~1x10^-18	
10 nm AlGaN-30% Al	x30	5 Å GaN: Si ~1x10^-18	x50
3.5 nm GaN: Si ~1x10^-18		10 Å AlGaN -30% Al	
13 nm AlN		0.3 um GaN: Si ~1x10^-18	
150 nm GaN: Si ~1x10^-18		20 nm AlN Buffer layer	
0.5 AlN Template		C-plane (0001) Sapphire	
C-plane (0001) Sapphire			
1297		1300	
13 Å GaN		13 Å GaN	
5 Å GaN: Si ~1x10^-18	x4	5 Å GaN: Si ~1x10^-18	x4
10 Å AlGaN -65% Al		10 Å AlGaN -65% Al	
1 um AlGaN-50% Al: Si ~1x10^-18		0.3 um GaN	
20 nm AlN Buffer layer		20 nm AlN Buffer layer	
C-plane (0001) Sapphire		C-plane (0001) Sapphire	

In the SEM images seen in Fig 4a-c, there were noticeable defects observed in the samples 1142 (Fig 4a) and 1145 (Fig 4c), which were both lacking IST. Consequently, sample 1144 (Fig 4b) visibly appeared to have fewer defects in its surface and exhibited ISTs. Through close observation of samples 1142 (Fig 4a) and 1145 (Fig 4c) visible defects and hexagonal voids are present respectively in each material's surface. Based on the observation of the intersubband transitions and the SEM images, we conclude that the quality of the surface morphology is not a good indication whether an IST is present in the sample or not. Again, the SEM technique does not provide useful information about the atomic structure of the quantum wells. At best, it provides useful information about cracks and gross defects, these may not necessarily deplete the intersubband transitions.

Optical absorption measurements below the bandgap enabled the determination of thin film thickness, since interference patterns are easily observed when the thin film uniformity is high. To make these measurements, a well developed technique discovered by Fabry and Perot was utilized [20]. By making use of the interference pattern (or fringes) produced by the transmission of light through two partly reflecting surfaces, one may determine thicknesses of the thin film in question. In this case, there is a thin film (active area) on the surface of a sapphire substrate. Both the thin film and substrate layer will transmit some amount of light, with the total transmission being attributed to both the active layer and substrate layer. The phase, dependent upon the optical path length, of the transmitted light from both the thin film and the substrate determine whether these

transmissions will add constructively or destructively, i.e., resulting in an interference pattern. With the refractive index and angle of incidence being known, the interference pattern observed facilitated the measurement of thin film thickness using the following relation:

$$d = \frac{N}{2n \cos \theta \left(\frac{1}{\lambda_1} - \frac{1}{\lambda_2} \right)} \quad (1)$$

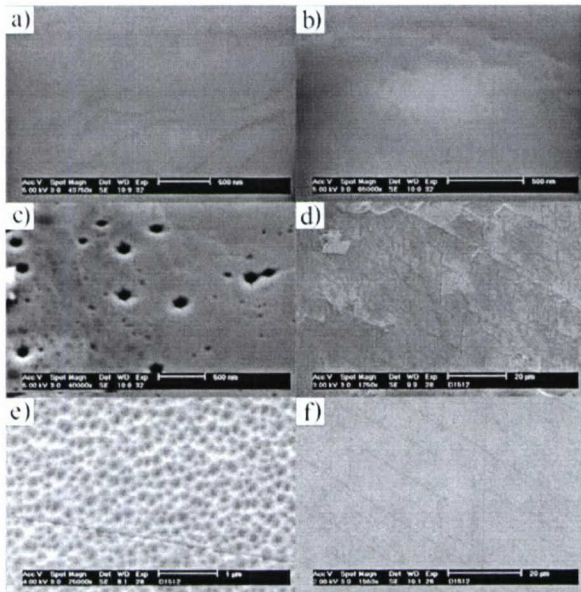


Figure 4: a) SEM image of sample 1142 with surface defects. b) SEM image of 1144 showing reduced defects. c) SEM image of sample 1145 with hexagonal voids. d) SEM image of sample 1297 with surface defects e) SEM image of sample 1293 with surface defects. f) SEM image of 1300 with surface defects. It may be noted that in fig 4d-f, it was not possible to significantly resolve the surface to achieve similar zoom factors as seen in fig 4a-c.

Where d is the thickness of the sample, N is the number of fringes between λ_1 and λ_2 , n is the refractive index of GaN (2.2), θ is the angle of incidence (zero degrees at normal). While it was possible to measure the overall thickness of the active layer in each structure, measurements of each individual epitaxial layer was not possible without the aide of a Transmission Electron Microscope (TEM). Due to the availability and preparation time required for these measurements, data collection is in progress and is not available in full at this time.

In the case of MBE growth, due to the limitations of the system, there were doubts that control of AlGaN growth was as predictable as needed. In the MBE system, control of the aluminum (Al) composition was controlled by adjusting the Al flux in the system. With requirements of higher aluminum compositions in some of the samples, higher temperatures were needed to get a large enough flux in the system. However the Al cell could not be raised to the necessary temperatures without damaging the cell itself. To overcome this obstacle, RF Nitrogen pressure was reduced to decrease the growth rate, thereby increasing Al composition. This solution proved helpful but also presented problems due to the instability of the RF N at such low pressures. Due to operating the system at the edge of normal operation, these factors have proven to be a hindrance in growth rate control and have introduced a noticeable amount of error in growth. Consequently, since the growth rate was reduced to some 60-80 nm per hour, the calibration of the system also proved tedious and is believed to introduce some inconsistencies due to this reduced/ unstable growth rate.

The presence of intersubband absorption in these structures has provided much insight into this phenomenon and has raised many questions about the causes limiting the optical properties of these materials. While there appears to be little correlation between surface morphology and the presence of ISTs, there may also prove to be other compromising factors limiting the optical properties of these materials. While additional tests such as thickness and bandgap measurements were useful in characterizing growth parameters, they do not offer supportive evidence of what may be limiting the optical properties of these materials. It is believed that other measurements outside the scope of this study may prove to be more useful in determining the unreliable optical properties encountered in these samples. Future plans are to further explain inconsistencies of the observed results through additional measurements such as TEM and X-ray satellite valley measurements. Nonetheless, while the data has proven that the presence of ISTs is considerably more complex than these mere morphological studies, the available data has given more direction in where future efforts must be focused to provide more compelling results. The overall goal is that continued research of this material will give a contributory understanding of what effects are limiting the optical properties of these materials so that the future of these materials may be fully realized.

6. Determination of the carrier concentration in InGaAsN/GaAs single quantum wells using Raman scattering.

Raman scattering from longitudinal optical phonon-plasmon coupled mode was observed in a series of InGaAsN/GaAs single-quantum-well samples grown by metalorganic vapor phase epitaxy. The phonon-plasmon mode spectra were fitted with the dielectric constant function based on Drude model that contains contributions from both lattice vibrations and conduction electrons. The carrier concentration is calculated directly from the plasmon frequency, which is obtained from the fitting procedure. An empirical expression for the electron concentration, [n], in InGaAsN/GaAs samples is determined as $[n] \approx \{2.35 \times 10^{16}(\omega_m - 502)\} \text{ cm}^{-3}$, where ω_m is the peak of the upper frequency branch, L_+ , of the phonon-plasmon mode measured in unit of cm^{-1} . The phonon-plasmon coupled mode was also investigated in rapid thermally annealed samples.

Dilute nitride materials such as InGaAsN have been the subject of intense investigation for their applications in multijunction photovoltaic and optoelectronic devices operating at 1.3 and 1.5 μm . This is due, in part, to the large bandgap bowing factor resulting from nitrogen incorporation in the material. For example, the addition of 2% nitrogen causes the bandgap to decrease by about 0.4eV. The ability to vary the bandgap of the alloy material in a wide range by optimizing the nitrogen content provides means to tailor the material properties for the desired device applications.

The determination of the conduction electrons concentration in diluted nitrides is very important for device fabrication. Hall effect is typically the method used for measuring the carrier concentration in semiconductors, which requires the fabrication of ohmic contacts. It is possible, however, to determine the carrier concentration in polar semiconductor materials using Raman scattering without the need of ohmic contacts. This is because the collective oscillation (plasmon) of free carriers can interact with the longitudinal optical (LO) phonons through the longitudinal electric fields and form an

LO-plasmon coupled (LOPC) mode. This mode was first demonstrated in GaAs bulk material⁸ and had been recently reported in n-type GaN thin films.

The Raman scattering intensity, $I(\omega)$, is related to the dielectric constant according to the following relation

$$I(\omega) \propto \text{Im} \left[-\frac{1}{\epsilon(\omega)} \right], \quad (1)$$

where $\epsilon(\omega)$ is the dielectric function consisting of phonon and plasmon contributions and is given by

$$\epsilon(\omega) = \epsilon_{\infty} \left(1 + \frac{\omega_L^2 - \omega_T^2}{\omega_T^2 - \omega^2 - i\omega\Gamma} - \frac{\omega_p^2}{\omega^2 - i\omega\gamma} \right), \quad (2)$$

where ϵ_{∞} is the high frequency dielectric constant and is approximately taken as the square of the refractive index at the probe laser wavelength used (1064 nm), ω_L is the LO phonon frequency (291cm^{-1}), ω_T is the TO phonon frequency (268 cm^{-1}), Γ is the phonon damping rate, γ is plasmon damping rate, and ω_p is the plasmon frequency given by

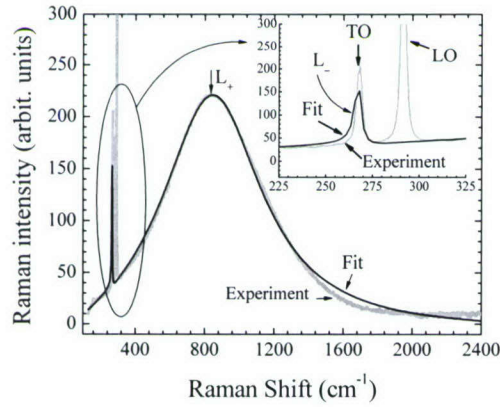
$$\omega_p^2 = \frac{ne^2}{\epsilon_0 \epsilon_{\infty} m^*}, \quad (3)$$

where n is the carrier concentration, e is the electric charge, ϵ_0 is permittivity of space, and m^* is the electron effective mass. Notice that LO and TO phonon frequency were obtained from the Raman measurements as shown in Fig. 1. These frequencies varied slightly from sample to sample, but they are in good agreement with the frequencies reported for InGaAsN. Furthermore, the measured phonon frequencies are slightly smaller than those reported for bulk GaAs materials. The LOPC mode splits into two modes known as L_+ and L_- branches. These two branches are approximately obtained by setting $\Gamma = \gamma = 0$ and solve Eq. (2) for $\epsilon(\omega) = 0$, which yields

$$L_{\pm} = \frac{1}{\sqrt{2}} \left[\left(\omega_L^2 + \omega_p^2 \right) \pm \sqrt{\left(\omega_L^2 + \omega_p^2 \right)^2 - 4\omega_T^2 \omega_p^2} \right]^{1/2}. \quad (4)$$

The GaAs/InGaAsN/GaAs single quantum well samples were grown by atmospheric-pressure metalorganic vapor phase epitaxy at $570\text{ }^{\circ}\text{C}$ on semi-insulating GaAs oriented 2 degrees from (100) to (110). A typical size of the substrate is $1\text{cm} \times 2\text{cm}$. Trimethylgallium, trimethylindium, arsine, and dimethylhydrazine (DMH) were used as precursors. The growth rate was 5 microns/h for the InGaAsN active layers. The N content was changed for the various samples by varying the DMH source flow rate and the In mole fraction was approximately 7% for all samples. The InGaAsN active layers were 100 \AA thick, and were clad on both sides by n-type GaAs doped with silicon from disilane precursor with doping level on the order of mid 10^{18}cm^{-3} . The cladding layers various in thickness Several of these samples were used in a previous photoluminescence study¹⁵ where the indium and the nitrogen contents were reported. The Raman scattering spectra were recorded at room temperature using a Fourier-transform spectrometer in conjunction with a YAG laser and an optics transfer attachment.

A typical Raman scattering spectrum of LOPC mode in InGaAs/GaAs single quantum well is shown in Fig. 1 as the gray spectrum. This spectrum was fitted with Eq. (1) and the result is shown as the thin black line. The fitting procedure reveals both L_+ and L_- . The L_- region along with the LO and TO phonon modes are replotted in the figure inset for clarity. The plasma frequency, ω_p , was used as one of the fitting parameters. The fitting procedure, illustrated in Fig. 1, was repeated for several samples, from which L_+ and ω_p were obtained. The frequency maximum of L_+ branch was obtained for the samples and plotted as a function of the plasmon frequency, as shown in Fig. 2. Equation (4) is also plotted in this figure (solid lines) along with the LO and TO phonon modes (dashed lines).



according to Eq. (3) for several samples. The frequency maximum, ω_m , of the LOPC mode upper branch is plotted as a function of the carrier concentration, as shown in Fig. 3. The solid line is the result of the linear fit of the data from which the following expression is obtained: $[n] = 2.35 \times 10^{16}(\omega_m - 502) \text{ cm}^{-3}$. This expression can be used to obtain the carrier concentration directly from the peak of L_+ mode, which is measured directly by Raman scattering in unit of cm^{-1} , as shown in Fig. 1.

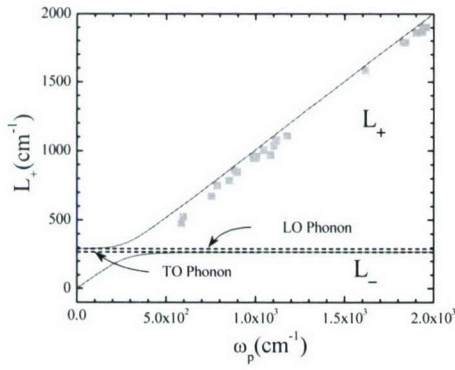


Fig. 2. A plot of the L_+ mode as a function of the plasmon frequency for a series of InGaAsN/GaAs single quantum well samples (solid squares). The plasmon frequency, ω_p , was obtained from fitting the LOPC mode in the samples. The solid lines are plots of L_+ and L_- given by Eq. (4). The dashed lines represent the LO and TO phonon frequencies.

Fig. 1. A Raman scattering spectrum obtained for an InGaAsN/GaAs single quantum well sample (gray line). The spectrum shows the LO, TO and the L_+ branch of the LOPC mode. The solid black line is the result of the fitting analysis using Eq. (1), which shows both the L_+ and L_- branched of the LOPC mode. The inset is the expansion of the spectral region in the vicinity of LO and TO phonon modes.

The carrier concentration, $[n]$, is calculated from the plasmon frequency

By measuring over 30 samples, The LOPC mode is mostly observed in InGaAsN/GaAs single quantum well samples. It is seldom that this mode is observed in doped InGaAsN/GaAs single heterojunction, i.e. silicon-doped InGaAsN layer grown on semi-insulating GaAs substrate with an n-type GaAs buffer layer. Thus, we believe that the LOPC mode is generated in the InGaAsN single quantum well, where the two-dimensional electron gas in the well is generated from the Si-doped GaAs cladding layers.

The carrier concentration in the solar cell active region is very important. One of the potential applications of diluted nitride materials, such as InGaAsN, is their use in multijunction solar cells. Therefore, the determination of the carrier concentration in this class of material is needed. In case of InGaAsN single quantum wells, the Hall effect measurements are very difficult to obtain since this technique cannot distinguish between various layers in the structure. On the other hand, Raman scattering from phonon-plasmon mode is very convenient method of determining the carrier concentration as described above. Additionally, micro-Raman is becoming a routine technique in determining the distribution of carrier concentrations in epitaxially grown layers. Hence, the results reported in Figs. 1-3 present a straight forward method of determining the carrier concentration in InGaAsN layers without the need of fabricating ohmic contacts.

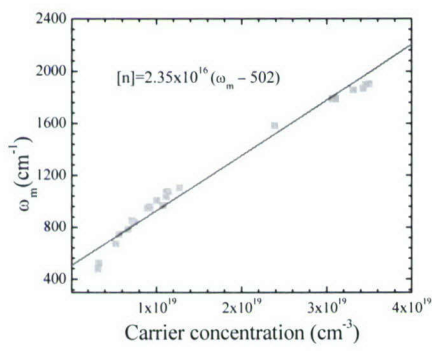
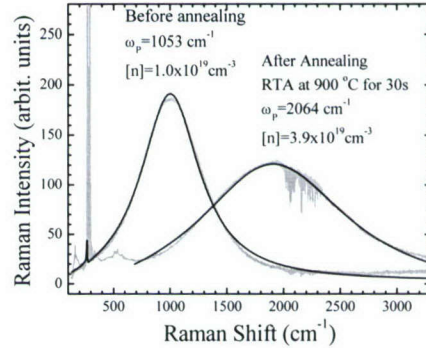


Fig. 3. The frequency maximum, ω_m , of L_+ branch as a function of the carrier concentration obtained from the data in Fig. 2. The solid line is a first order linear fit of the data.

Another test of the LOPC mode in InGaAsN/GaAs single quantum well samples is the thermal annealing. Both furnace annealing and rapid thermal annealing (RTA) have a drastic effect on the carrier concentration in

semiconductor including diluted nitrides. Several InGaAsN/GaAs single quantum well samples were annealed using an RTA set-up. A typical result of the RTA effect on the LOPC mode is shown in Fig. 4, where the Raman scattering spectra (gray lines) are recorded for two pieces cut from the same wafer, of which one was annealed at $900\text{ }^\circ\text{C}$ for 30 s and the other was unannealed. It is clear from this figure that a large blue-shift is observed for the LOPC mode in the annealed sample. This behavior is observed in all annealed samples. Both spectra were fitted using Eq. (1) and the fitted lines are displayed as the thin black lines. The plasmon frequencies obtained from the fitting procedure are 1053 cm^{-1} and 2054 cm^{-1} for the unannealed and annealed samples, respectively, with accuracy less than 0.5% as obtained from the fitting results. The corresponding carrier concentrations are $1.0 \times 10^{19}\text{ cm}^{-3}$ for the unannealed sample and $3.9 \times 10^{19}\text{ cm}^{-3}$ for the annealed sample, an increase of a factor of 3.9.

Fig. 4. Rapid thermal annealing effect on the LOPC mode in InGaAsN/GaAs single quantum well. The gray lines represent the Raman scattering spectra obtained for unannealed and annealed samples cut from the same wafer. The thin black lines represent the results of the fitting analysis.



A plausible explanation of the increase of the carrier concentration in the annealed sample is that many of the defects, imperfections, and traps in the structure are annealed out releasing the electrons to the conduction band. It is obvious that the increase of the carrier concentration causes the blue-shift of the LOPC mode, which is demonstrated experimentally in Fig. 4.

It is noted that the full width at half maximum of the spectrum obtained for the annealed sample in Fig. 4 is larger than that of the unannealed sample. This is translated into a larger plasmon damping rate, γ , which is also used in the fitting analysis. The γ values obtained for the Raman spectra in Fig. 4 are 634 and 1549 cm⁻¹ before and after annealing, respectively, with accuracy less than 0.5% as obtained from fitting results. The plasmon damping rate is related to the carrier drift mobility, μ , through the following relation: $\mu = e/(m^* \gamma)$. Thus, the carrier mobility in the annealed sample is about a factor 2.44 smaller than that of the unannealed sample.

One possible explanation of the reduction of the mobility is the electron-electron scattering, which is significant for systems with carrier concentration larger than 10¹⁸ cm⁻³. The electron-electron scattering increases as the electron concentration is increased. Hence, the carrier drift mobility decreases as the electron-electron scattering is increased. The drift mobility values estimated from the plasmon damping rate are ~220 cm².V⁻¹.s⁻¹ and ~90 cm².V⁻¹.s⁻¹ for the unannealed and annealed samples, respectively. While the above explanation is a plausible reason, there are other scattering mechanisms that may affect the mobility.

These mobility values are in good agreement with those reported by Young *et al.*²⁴ The electron effective mass was chosen as 0.067 m_o, which is the effective mass in the bulk GaAs material, in our estimation of the carrier concentration [see Eq. (3)] and the drift mobility. For InGaAsN material, the effective mass is still surrounded by controversy. Recent reports show that the electron effective mass is ranging between ~(0.1 - 0.5)m_o, while other reports indicate that the electron effective mass is in the range of ~(0.004 – 0.11)m_o. Thus, our choice of m* is in agreement with the latter range.

In conclusion, the Raman scattering from longitudinal optical phonon – plasmon coupled mode is investigated in a series of InGaAsN/GaAs single quantum well samples. A Drude based dielectric constant, which contains contribution from lattice vibrations and plasmon, is used for the line-shape fitting analysis of Raman spectra. The plasmon frequency was extracted from the analysis and used to calculate the electron concentrations in the samples. An empirical expression for the carrier concentration as a function of the frequency maximum of the LOPC coupled mode upper branch is obtained, which allows one to directly estimate the carrier concentration from the Raman scattering spectra. Rapid thermal annealing reveals a significant increase in the LOPC mode frequency, which is translated to a significant increase in the carrier concentration in the annealed samples. The increase of the carrier concentration in the annealed samples is accompanied by an increase in the plasmon damping rate, which leads to a decrease in the carrier drift mobility.

7. Longitudinal Modes in InAlGaAs/AlGaAs High-Power Laser Diodes:

The emission from bias voltage driven In_{0.06}Al_{0.08}Ga_{0.86}As/Al_{0.3}Ga_{0.7}As edge-emitting diode lasers with cavity lengths of 0.6 and 0.9 mm was measured at 290 K using a high resolution Fourier-transform infrared spectrometer. The light-current (L-I)

characteristic curves showed that a threshold current of ~ 0.5 and 0.8 A was needed to reach the stimulated emission in laser diodes with cavity lengths of 0.6 and 0.9 mm, respectively. The laser diode longitudinal modes were observed in the stimulated emission spectrum for each of the devices. These spectra enabled us to calculate the refractive index, total loss, and gain of the active region. On the other hand, the cavity length was determined by utilizing the interferogram spectrum, longitudinal modes spacing, and direct measurements of the laser dimensions. A good agreement between the cavity length values obtained from the three methods was achieved.

High-power laser diodes currently serve as efficient optical pumps for solid-state lasers and become more important as direct tools for material processing, including soldering and welding of metals. The characterization of lasers is a research topic of ongoing relevance and importance, which has played a major role in the development of new laser materials and the design of laser structures. High efficiency lasers in the infrared range are an essential part in developing high-power laser diodes.

One feature of laser diodes is the longitudinal mode distribution. It has been observed previously that the laser emission spectra have periodic spaced intervals. In this paper, we report on the measurements of the longitudinal modes of the edge-emitting InAlGaAs/AlGaAs single quantum well laser diodes. By measuring the actual length of the laser diode using a micrometer and by measuring the separations between the longitudinal modes, we obtained the refractive index of the laser active region. In addition to the direct measurements of the laser diode dimensions, the laser cavity length was obtained directly by measuring the spacing between the peaks observed in the interferogram spectrum. The overall cavity loss factor was obtained from the full width at half maximum of the longitudinal modes peaks.

The devices that were characterized are based on an $In_{0.06}Al_{0.08}Ga_{0.86}As/Al_{0.3}Ga_{0.7}As$ single quantum well (SQW), which have been grown by metalorganic vapor deposition on *n*-type GaAs substrates. The devices consist of an array of twenty $4\text{ }\mu\text{m}$ wide stripes which were fabricated on the p-type side of the laser diode. The lasers were then packaged by mounting the p-type side down on a copper heat sink. Gold wire bonding was performed to complete the packaging process.

One of the most important characteristics of a laser diode is the amount of light it emits as current is injected into the device. The L-I measurements determine the output power with respect to the input current. A bias current ranging from 0 to 2 A was applied to the laser diodes. Using a power meter, the output power of the laser emission was measured as the input current was increased. From this characterization method the threshold current, slope efficiency, and external quantum efficiency were obtained.

A Bomem DA8 Fourier-transform spectrometer was used to determine the emission wavelength, intensity, and longitudinal modes of the output signal. These laser devices were enclosed in a continuous flow cryostat under vacuum maintained at a constant temperature of 290.0 ± 0.3 K. These measurements were taken at a resolution of 0.1 cm^{-1} , where the input current was 1.1 A. Ultimately, with the use of these spectra of the stimulated emission intensity, the refractive index of the laser was calculated. Using the interferogram results, periodic peaks within the spectra of data points can be measured which correspond to the cavity length of the devices. For comparison, the cavity lengths of the 0.6 and 0.9 mm long lasers were measured using a digital micrometer and obtained by measuring the separation between the longitudinal modes.

The output power of the laser diodes was measured as a function of the bias current and the results are shown in Fig. 1 for two devices with different cavity lengths. The data in this figure illustrates the typical laser behavior where the boundary between the spontaneous and stimulated emissions is represented by the threshold current (I_{th}). The threshold currents for the 0.6 and 0.9 mm long lasers was approximately 0.5 and 0.8 A, respectively. The region between the threshold current and the maximum output power is when stimulated emission or lasing occurs. By applying linear fit analysis to this region, the slope efficiency (η_{slope}) can be measured and, sequentially, the external quantum efficiency (η_{ext}) can be calculated according to the following expression

$$\eta_{ext} = \eta_{slope} \frac{q\lambda_o}{hc}, \quad (1)$$

where q is the charge of an electron, λ_o is the emission wavelength, h is Planck's constant, c is the speed of light, and η_{slope} is the slope efficiency. The emission wavelength, λ_o , for the 0.6 and 0.9 mm long devices was approximately 0.814 and 0.8097 μm , respectively. From this equation, the external quantum efficiency for the 0.6 and 0.9 mm long devices was 43% and 68%, respectively.

The threshold current plays an important role in the operation of semiconductor lasers. Above I_{th} , stimulated emission dominates over spontaneous emission, generating a well defined peak shown in Fig. 2. It has been revealed that at a high resolution periodic longitudinal modes can be measured. The resolution used to obtain the spectral modes was 0.1 cm^{-1} . Longitudinal modes are standing waves that propagate perpendicularly to the mirror facets traveling from one mirror to another without

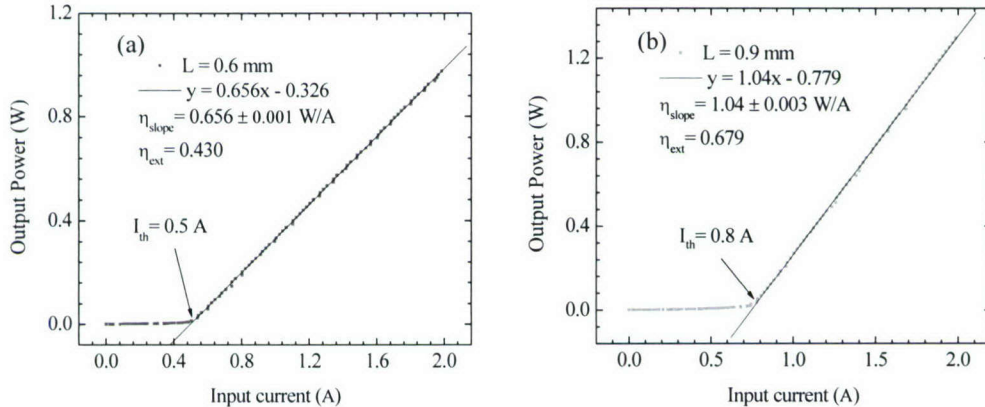


Fig. 1. Light power as a function of the applied bias current plotted for an $\text{In}_{0.06}\text{Al}_{0.08}\text{Ga}_{0.86}\text{As}/\text{Al}_{0.3}\text{Ga}_{0.7}\text{As}$ quantum well laser diode under continuous-wave room temperature operation for a (a) 0.6 and (b) 0.9 mm long device.

escaping from the resonator. Figure 2 displays a narrow peak with an emission wavelength maximum at approximately 0.8097 μm by applying an injection current of 1.1 A.

As photons travel through the active region, losses occur due to finite mirror transmission and absorption. The total loss within the cavity is directly related to the efficiency of a laser diode. Structures that have lower losses will have higher

efficiencies. The finesse is a measure of the contrast of the resonator and can be defined as

$$F = \frac{\pi\sqrt{\gamma}}{(1-\gamma)}, \quad (2)$$

where γ is the total loss within the cavity. The longitudinal mode spectral distribution has a full width at half-maximum ($\Delta\omega_{long}$) equal to

$$\Delta\omega_{long} = \frac{\pi c}{LF}, \quad (3)$$

where L is cavity length. If the finesse is calculated using equation (3), then the total loss can be obtained by applying equation (2). Since $\Delta\omega_{long}$ varies between the peaks, average values must be used for the total loss and finesse. The total loss and finesse for the 0.9 mm long laser diode was calculated to be 0.72 ± 0.01 per unit length and 9.51 ± 0.28 , respectively. The confinement factor characterizes a portion of the light energy accumulated within the active layer where the phototransitions take place and is expressed in the following relation

$$\Gamma = 2\pi^2 \left(n_a^2 - n_b^2 \right) \frac{d^2}{\lambda_o^2}, \quad (4)$$

where n_a is the refractive index of the active layer, n_b is refractive index of the barrier, and d is the quantum well width. The refractive index used for the active layer was 4.05, while the refractive index used for the barrier was 3.46. The quantum well width was approximately 7 nm. From these values, the confinement factor defined in equation (4) was determined to be 0.007. The gain in the medium is the ratio of the total loss to the

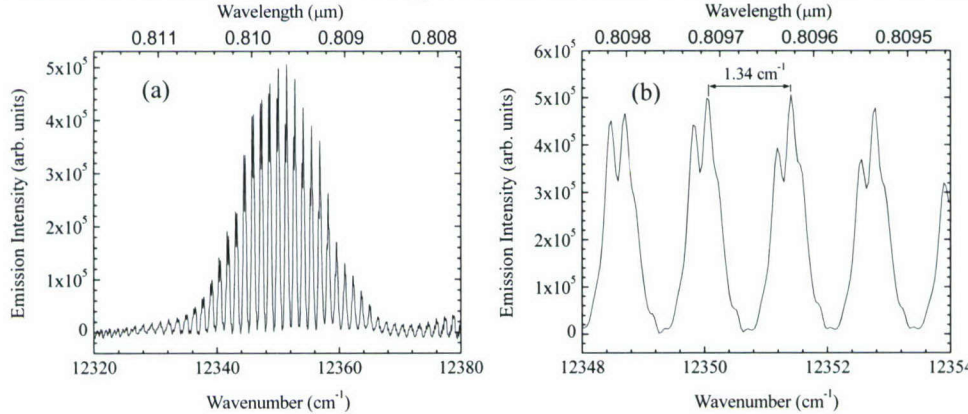


Fig. 2. (a) A stimulated emission spectra for an $In_{0.06}Al_{0.08}Ga_{0.86}As/Al_{0.3}Ga_{0.7}As$ quantum well laser diode with a cavity length of 0.9 mm and (b) an expanded longitudinal mode region with spacing of 1.34 cm^{-1} .

confinement factor

$$g = \frac{\gamma}{\Gamma}, \quad (5)$$

which was calculated to be 109.74 ± 1.04 per unit length.

A laser spectrum is shaped in accordance with the gain of the active material and the oscillating frequencies of the resonator. The optical waves propagating through the laser cavity form standing waves between the two mirror facets of the laser. The period of

oscillation of this curve is determined by the distance L between the two mirrors. Hence, a node must exist at each end of the cavity where the amplitude of the wave must be zero. The only way this can take place is for L to be a multiple of half wavelengths, $\lambda/2$. This means that the cavity length can be represented by the ensuing relation

$$L = \frac{m\lambda_o}{2n_a}, \quad (6)$$

where m is an integer reflecting the number of modes. Longitudinal modes are formed from multiple reflections within the laser cavity due to the two facets of the edge-emitting laser. As a result of this situation there can exist many longitudinal modes in the cavity of the laser diode each resonating at its distinct wavelength. Thus, the spacing of the longitudinal modes is inversely proportional to the cavity length and can be derived from equation (6) as

$$\Delta\lambda = \frac{\lambda_0^2}{2n_a L}, \quad (7)$$

where $\Delta\lambda$ is the wavelength separation between the longitudinal modes. The refractive index of the active layer of the structure can be determined from the above relation. Knowing the $\Delta\lambda$, λ_o , and λ allows one to obtain the refractive index n_a . A refractive index of 4.05 was calculated using this relation. This value is comparable to the refractive index of 3.648 for GaAs at room temperature. As a result of the Al and In content in the active well region, it is expected to have a slightly higher value of n_a for $\text{In}_{0.06}\text{Al}_{0.08}\text{Ga}_{0.86}\text{As}$.

Since the Fourier-transform spectrometer applies the Fourier-transform of the interferogram to acquire the emission spectra, it is possible that the interferogram can be utilized to measure the cavity length. The interferogram spectrum was shifted so that the first data point was zero and evenly spaced periodic peaks were observed corresponding to the laser cavity length. The interferogram results for a laser diode with a nominal cavity length of 0.9 mm are displayed in Fig 3.

To evaluate the accuracy of this method, the cavity lengths of various laser diodes were determined using two other techniques. A microscope with a digital micrometer was the first method used to measure the cavity length. The second technique used for comparison was transforming equation (6) so that the difference in the angular frequency is inversely proportional to the cavity length as shown below

$$\Delta\omega = \frac{\pi c}{Ln_a}. \quad (8)$$

The mode spacing in wavenumbers was obtained from Fig. 2 and then converted in order to determine the mode spacing in angular frequency ($\Delta\omega$). Finally, the cavity length can be calculated by using equation (8). The cavity length results for the three methods discussed above are shown in Table I. As this table indicates, good agreement is obtained for the cavity length of six different devices using three different methods. The errors reported for the data are due to the variation of $\Delta\omega$.

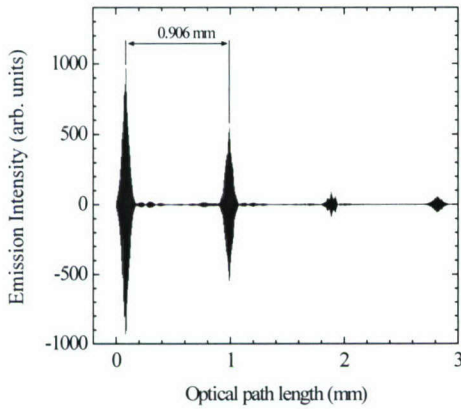


Fig. 3. The interferogram spectrum from which the emission spectrum in Fig. 2 is obtained. The separation between the peaks was found to be 0.906 mm.

Table I. Cavity Length Measurements for the Different Methods

Device	Micrometer Measurement (mm)	Interferogram Measurement (mm)	Equation Calculation (mm)	(8)
1	0.908 ± 0.001	0.920 ± 0.009	0.926 ± 0.009	
2	0.909 ± 0.001	0.917 ± 0.007	0.926 ± 0.011	
3	0.909 ± 0.001	0.913 ± 0.012	0.921 ± 0.014	
4	0.908 ± 0.001	0.909 ± 0.025	0.921 ± 0.014	
5	0.608 ± 0.001	0.584 ± 0.006	0.596 ± 0.005	
6	0.611 ± 0.001	0.589 ± 0.029	0.636 ± 0.072	

In summary, the external quantum efficiency, refractive index, emission wavelength, total cavity loss, active layer gain, and cavity length were all determined for the high-power $\text{In}_{0.06}\text{Al}_{0.08}\text{Ga}_{0.86}\text{As}/\text{Al}_{0.3}\text{Ga}_{0.7}\text{As}$ edge-emitting laser diodes. The external quantum efficiencies for the 0.6 and 0.9 mm long laser diodes were found to be 43% and 68%, respectively. A refractive index of approximately 4 was calculated for the active layer. The emission wavelength for the 0.6 and 0.9 mm long devices was approximately 0.814 and 0.8097 μm , respectively. A good agreement between the cavity length measurement methods was achieved for laser diodes with regular periodic spaced longitudinal modes within the emission spectra. The purpose of fully understanding the characterization methods previously discussed is that by manipulating the semiconductor material and the cavity length, the design of a wide range of emission wavelengths are achievable. Thus, these characterization approaches seem promising for a wide variety of semiconductor laser designs.

8. List of publications, professional activities and students:

A. Papers in technical journals and symposia:

1. “Investigation of indium distribution in InGaAs/GaAs quantum dot stacks using high-resolution x-ray diffraction and Raman scattering,” Yu. I. Mazur, Zh. M. Wang, G. J. Salamo, V. V. Strelchuk, V. P. Kladko, V. F. Machulin, M. Ya. Valakh, and M. O. Manasreh, *J. Appl. Phys.* **99**, 023517-1 (2006).
2. “Investigation of rapid thermal annealing on Cu(In,Ga)Se₂ films and solar cells,” X. Wang, S. S. Li, K. W. Kim, S. Yoon, V. Cracium, J. M. Howard, S. M. O. Manasreh, O. D. Crisalle,, and T. J. Anderson, *Journal of Solar Materials and Solar cells* (accepted).
3. “Broadband photoresponse from InAs quantum dots embedded in InGaAs graded well,” J. Liang, M. O. Manasreh, E. Marega, Jr., and G. J Salamo, *IEEE Electron Device Letters Vol.* **26**, 631-633, (2005).
4. “Intersubband transitions in proton irradiated InGaAs/GaAs multiple quantum dots,” Y. C. Chua, E. A. decuir, Jr., M. O. Manasreh, and B. D. Weaver, *Appl. Phys. Lett.* **87**, No. 9, 091905 (3 pages) (2005).
5. “Investigation of pulsed laser annealing (PLA) and rapid thermal annealing (RTA) of CIGS films and solar cells,” Xuege Wang, Sheng. S. Li, V. Craciun, W. K. Kim, S. Yoon, J. M. Howard, M. O. Manasreh, J.Venturini, O. D. Crisalle, and T. J. Anderson. *IEEE 31st Photovoltaic Specialists Conference (PVSC)*, Orlando, Florida (January 2005).
6. “Proton irradiation effect on single-wall carbon nanotubes in a poly(3-octylthiophene) matrix” P. P. Neupane and M. O. Manasreh, B. D. Weaver, R.P. Rafaelle, and B.J. Landi, *Appl. Phys. Lett.* **86**, 221908-22190 (2005).
7. “Intersubband transition in GaN/AlGaN multi-quantum wells,” E. A. Decuir, Y. C. Chua, B. S. Passmore, J. Liang, J. Xie, H. Morkoç, A. Payne, and I. T. Ferguson, *Materials Research Society, Vol.* **829**, 175-181 (2005).
8. “Spectroscopic analysis of external stresses in semiconductor quantum-well materials,” Jens W. Tomm, Mark L. Biermann, B. S. Passmore, M. O. Manasreh, A. Gerhardt, and Tran Q. Tien, *Materials Research Society, Vol.* **829**, 233-242 (2005). Invited.
9. “Intersubband Transitions in In_{0.3}Ga_{0.7}As/GaAs Multiple Quantum of Varying Dot-Sizes,” Y.C. Chua, Jie Liang, B.S. Passmore, E. A. Decuir, M.O. Manasreh, Zhiming Wang, and G.J. Salamo, *Materials Research Society, Vol.* **829**, 15-20 (2005).
10. “Longitudinal Modes in InAlGaAs/GaAs High-Power Laser Diodes,” B. S. Passmore, S. C. Chua, M. O. Manasreh, and J. W. Tomm, *Materials Research Society, Vol.* **829**, 87-92 (2005).

11. "Tuning $In_{0.3}Ga_{0.7}As/GaAs$ multiple quantum dots for long wavelength infrared detectors", Ying Chao Chua, E. A. Decuir, Jr., B. S. Passmore, K. H. Sharif, and M. O. Manasreh, Z. M. Wang and G. J. Salamo, Appl. Phys. Lett. **85**, 1003-1005 (2004). Selected for Virtual Journal of Nanoscale Science & Technology--August 16, Vol. **10**, Issue 7 (2004) <http://www.vjnano.org>
12. "Determination of the carrier concentration in $InGaAsN/GaAs$ single quantum wells using Raman scattering," Patrick. A. Grandt, Aureus E. Griffith, M. O. Manasreh, D. J. Friedman, S. Doğan, and D. Johnstone, Appl. Phys. Lett. **85**, 4905-4907 (2004).
13. "Infrared Optical Absorbance of Intersubband Transitions in $GaN/AlGaN$ Multiple Quantum Well Structures." Qiaoying Zhou, B. Pattada, Jiayu Chen, M. O. Manasreh, Faxian Xiu, Steve Puntigan, L. He, K. S. Ramaiah, and Hadis Morkoç, J. Appl. Phys. **94**, 10140-10142 (2003) Selected for Virtual Journal of Nanoscale Science & Technology--June 09, Vol. 7, Issue 23 (2003) <http://www.vjnano.org>
14. "Optical Absorption of Intersubband Transitions in $In_{0.3}Ga_{0.7}As/GaAs$ Multiple Quantum Dots." B. Pattada, Jiayu Chen, Qiaoying Zhou, M. O. Manasreh, M. Hussien, W. Ma, and G. J. Salamo, Appl. Phys. Lett. **82**, 2509-2511 (2003). Selected for Virtual Journal of Nanoscale Science & Technology--April 21, Volume 7, Issue 16 (2003) <http://www.vjnano.org>
15. "Normal Incident Infrared Intersubband Transitions of $InGaAs/GaAs$ quantum dots." Mohammad Hussein, Wenquan Ma, M. O. Manasreh, and G. J. Salamo, Material Research Society Spring Meeting 2003, Symposium Q.
16. "Intersubband transitions in Proton Irradiated $InGaAs/InAlAs$, Multiple Quantum Wells Grown in Lattice Matched InP Substrates." Qiaoying Zhou, M. O. Manasreh, B. D. Weaver, and M. Missous, Materials Research Society, Vol. **744**, 301-307 (2003).
17. "Intersubband Transitions in $In_xGa_{1-x}As/AlGaAs$ Multiple Quantum Wells for Long Wavelength Infrared Detection." Clayton L. Workman, Zhiming Wang, Wenquan Ma, Christi E. George, R. Paneer Selvam, Gregory J. Salamo, Qiaoying Zhou, and M. O. Manasreh, Material Research Society, Materials Research Society, Vol. **744**, 607-612 (2003).
18. "Interband transitions in $GaInNAs/GaAs$ Single Quantum Wells", M. O. Manasreh, D. J. Friedman, W. Q. Ma, C. L. Workman, C. E. George, and G. J. Salamo, Material Research Society, Materials Research Society, Vol. **744**, 647-652 (2003).
19. "Phonon Modes of GaN/AlN Heterojunction Field Effect Transistor Structures Grown on Si(111) Substrates." B. Pattada, Jiayu Chen, M. O. Manasreh, S. Guo, and B. Peres, J. Appl. Phys. **93**, 5824-5826 (2003). Rapid Communication.
20. "Photoluminescence of Metalorganic Chemical Vapor Deposition Grown $GaInNAs/GaAs$ Single Quantum Wells." M. O. Manasreh, D. J. Friedman, W. Q. Ma, C. L. Workman, C. E. George, and G. J. Salamo, Appl. Phys. Lett. **82**, 514-516 (2003).

B. Books and Symposia:

1. “**Semiconductor Heterojunctions and Nanostructures**,” Omar Manasreh (McGraw-Hill, New York, 2005). A textbook for graduate courses (554 pages).
2. “**Semiconductor materials and devices.**” A book series published by Artech House and edited by M. O. Manasreh.
Volume 1: “*SiC Devices and Technology*.” Edited by S. Saddow (2004)
Volume 2: “*Self-assembly Quantum Dots*.” Edited by T. Steiner, (2005).
volume 3: “*Optics of Quantum Dots and Wires*.” Edited by G. Bryant and J. Solomon, (2005).
Volume 4. “*Nanotechnology Applications to Telecommunications and Networking*.” Edited by D. Minoli, (2005).
3. “**Nanoscience and Technology**,” A new book series edited by M. O. Manasreh and published by McGraw-Hill and includes the following volumes:
“*Molecular Thermodynamics and Transport*” by M. H. Peters (2004)
“*MEMS/MOEM Packaging*” by K. Gilleo (2005)
“*Microfluid Mechanics*” by W. W. Liou and Y. Fang (2005)
“*Mechanical design of Microsensors*” by N. O. Lobontiu (in press)
“*Intersubband transitions in Quantum Structures*” by R. Paiella (in press)
“*Polymer Nanocomposites*” by J. K. Koo (in press).
“*Quantum-Well High-Power Laser Arrays*” by J. W. Tomm and J. Jimenez (in press).
5. “**Progress in Semiconductor Materials IV: Electronic & Optoelectronic Applications.**” A symposium is organized by Gail J. Brown, M. O. Manasreh, B. Biefeld, and C. Gmachl for the Materials Research Society (Fall 2004). Vol. **829**.
6. “**Progress in Semiconductor Materials III: Electronic & Optoelectronic Applications.**” A symposium is organized by D. Friedman, M. O. Manasreh, Irina Buyanova, and J. Auret for the Materials Research Society (Fall 2003), Vol. **799**.

C. Professional Papers at Regional, National, and International Meetings:

21. “*Investigation of pulsed laser annealing (PLA) and rapid thermal annealing (RTA) of CIGS films and solar cells*,” Xuege Wang, Sheng. S. Li, V. Craciun, W. K. Kim, S. Yoon, J. M. Howard, M. O. Manasreh, J. Venturini, O. D. Crisalle, and T. J. Anderson. IEEE 31st Photovoltaic Specialists Conference (PVSC), Orlando, Florida (January 2005). Oral presentation.
22. “*Intersubband transition in GaN/AlGaN multi-quantum wells*,” E. A. Decuir, Y. C. Chua, B. S. Passmore, J. Liang, J. Xie, H. Morkoç, A. Payne, and I. T. Ferguson, Materials Research Society, Fall Meeting (2004). Poster.
23. “*Spectroscopic analysis of external stresses in semiconductor quantum-well materials*,” Jens W. Tomm, Mark L. Biermann, B. S. Passmore, M. O. Manasreh, A. Gerhardt, and Tran Q. Tien, Materials Research Society, Fall Meeting (2004). Invited.
24. “*Intersubband Transitions in In_{0.3}Ga_{0.7}As/GaAs Multiple Quantum of Varying Dot-Sizes*,” Y.C. Chua, Jie Liang, B.S. Passmore, E. A. Decuir, Jr., M.O. Manasreh, Zhiming Wang, and G.J. Salamo, Materials Research Society, Fall Meeting (2004). Oral presentation.

25. "Longitudinal Modes in InAlGaAs/GaAs High-Power Laser Diodes," B. S. Passmore, S. C. Chua, M. O. Manasreh, and J. W. Tomm, Materials Research Society, Fall Meeting (2004). Poster.

D. Invited Talks and Presentations:

1. "Optoelectronic Applications of III-V Semiconductor Nanostructures." A colloquium presented to the department of physics, University of Arkansas, 12/03/2004.
2. "Infrared Applications of III-V semiconductor Nanostructures." Presented at the Arkansas EPSCoR Annual Meeting, 9/24/2004.
3. "Infrared Applications of III-Nitride Multiple Quantum wells." An invited talk presented at the "Workshop on Nanoscale Issues Nitride Semiconductors," 23-26 August 2004 at the Anchorage Marriott Downtown, in Anchorage, Alaska.
4. "Quantum Well Infrared Photodetectors." Presented to Lockheed-Martin, Dallas, Texas, 8/5/2004.
5. "Optical Properties of III-V Quantum dots." Presented during the AFOSR Program Review, Anaheim, CA, 11-12 January (2003)

E. Students supported by the grant:

Name	Degree	Title of Thesis or Dissertation	Year Awarded or expected
Brandone Passmore	M.S.	Properties of high-power edge-emitting laser diode fabricated from In _{0.06} Al _{0.08} Ga _{0.84} As/Al _{0.3} Ga _{0.7} As single quantum well	May 2005
Simpson Shua	M. S.	Multiple quantum dot infrared detectors	May 2005
Eric DeCuir, Jr.	M.S.	Characterization of intersubband transitions in AlGaN/GaN multiple quantum well structures for near infrared detector applications	May 2005
Jie Liang	M.S.	Infrared photodetectors based on III-V semiconductor Quantum wells and dots	Dec 2005
Pranaya Neupane	M.S.	Radiation effect on single wall carbon nanotubes	May 2006
Avinash Muddasani	M. S.	ECV measurements in Quantum wells and dots	08/2006
Emil Fred	M.S.	(expected to go for Ph.D.). III-Nitride MQWs	05/2007
Yadav Kaushik Narsingi	M. S	II-VI Nanocrystals	05/2007
Chary Ravi Vadla	M.S.	ECV measurements	05/2007
Brandone Passmore	Ph.D.	Multicolor long wavelength detectors	05/2008
Eric DeCuir, Jr.	Ph.D.	Growth of III-Nitrides	05/2008
Robert Edger Nowlin	Ph.D.	Optical Communication	05/2009
Abi Joshi	B.S.	Fabrication of optoelectronic devices	05/2007